INNOVATIVE REMOTE SPECTROSCOPIC TECHNIQUES FOR PLANETARY EXPLORATION

A dissertation submitted to the graduate division
of the University of Hawai'i at Mānoa in partial fulfillment
of the requirements for the degree of

DOCTOR OF PHILOSOPHY

in

EARTH AND PLANETARY SCIENCE

August 2020

By
Macey W. Sandford

Dissertation Committee
Shiv K. Sharma (chairperson)
Paul G. Lucey
Robert Wright
Sarah Fagents
Jonathan Williams

This dissertation is dedicated to **exploration**; may we never stop striving to learn more, to do better, and to keep humbly moving forward.

Do Not Go Gentle into That Good Night
Dylan Thomas
Do not go gentle into that good night,
Old age should burn and rave at close of day;
Rage, rage against the dying of the light.

Though wise men at their end know dark is right,
Because their words had forked no lightning they
Do not go gentle into that good night.

Good men, the last wave by, crying how bright
Their frail deeds might have danced in a green bay,
Rage, rage against the dying of the light.

Wild men who caught and sang the sun in flight,
And learn, too late, they grieved it on its way,
Do not go gentle into that good night.

Grave men, near death, who see with blinding sight
Blind eyes could blaze like meteors and be gay,
Rage, rage against the dying of the light.

And you, my father, there on the sad height,
Curse, bless, me now with your fierce tears, I pray.
Do not go gentle into that good night.
Rage, rage against the dying of the light.

Acknowledgements

First and foremost, I would like to acknowledge and appreciate the opportunities that I have been given throughout my life. The year 2020 will surely go down in history as an eventful year and, as of now, it is only halfway over. The wildfires in Australia highlighted the consequences of climate change. The novel coronavirus has affected the entire world, showing us that we are all one humankind, but healthcare is still not a human right. The murder of George Floyd has ignited a revolution throughout the world to dismantle systematic racism, fueled by the Black Lives Matter movement. The privilege I have to be safe, healthy, and to not be judged based on the color of my skin, all while earning the highest academic degree, is acknowledged here. In fact, it has fueled my concentration these past several months as the world around me seems to catch fire over and over again. I want this dissertation to not only act as a testimony of the hard work I have accomplished over the past three years, but also as a testimony of my dedication to ensuring positive change in the world around me. I will continue to learn, give, teach, and explore. I promise to seek out those often overlooked and to empower them to continue to make positive change.

Without my family and close friends, I would not be where I am today. I would like to thank them for always supporting and believing in me. I would like to thank my father for instilling curiosity and confidence in me at a young age, my mother for never letting me believe that something is impossible, my brother for giving me someone to look up to and be challenged by, and my grandparents for setting me up for success by beating the odds during their respective lifetimes. I would also like to thank my partner for continuing to cheer me on when I stay strong and to pick me up when I fall down.

In particular, I wish to thank my advisor, Dr. Shiv Sharma, for his continued support and earnest enthusiasm for me to learn more. I also wish to thank Dr. Anupam Misra for his positivity and willingness to always share his knowledge with me. I could not be more grateful for my sudo-advisor, Dr. Paul Lucey, who has guided and supported me endlessly along my journey through graduate school. I would also like to thank each of my committee members not yet mentioned, Rob Wright, Sarah Fagents, and Jonathan Williams, for their support throughout this process. To all my colleagues in office 512, I could not have gotten to this day without the smiles, tears, and growth we have experienced with one another.

Abstract

This dissertation describes research involving three basic aspects of planetary missions using spectroscopic techniques for planetary exploration, namely instrumentation development, scientific qualification of instrumentation, and prioritization of data returned to Earth. The first chapter of this dissertation introduces the basic topics that are involved in the subsequent chapters. The second chapter describes the development and value of a compact portable remote Raman spectrometer that collects spectra of targets hundreds of meters away. This project validated the system and displayed a technological advance in the field as the farthest Raman measurement yet using a compact Raman system. The third chapter uses the same instrumentation developed in chapter 2 to validate the use of Raman spectroscopy in the exploration of ocean worlds. Ocean worlds are found in the outer Solar System and have been at the center of habitability studies over the past few decades. In order for instrumentation to be applicable onboard a mission payload, it must be capable of measuring samples relevant to the science goals of that mission. By procuring and measuring ocean world relevant samples, I convince the audience that a remote Raman spectrometer is a scientifically valuable tool for inclusion on a mission to the surface of an ocean world. The final part of this dissertation deals with the processing of data once it is collected. Hyperspectral imaging spectrometers characterize surfaces by the absorption features resulting from the interaction of light with a planetary surface. The absorption features are specific to the characteristics of the surface from which light was reflected from. These spectrometers are valuable due to their ability to sample from orbit with high spectral and spatial resolution. In the same thread, these instruments produce ever-growing datasets that often surpass the available return bandwidth. In order to improve the science that a mission conducts, it is essential to retrieve as much scientifically relevant data as possible. One way to bypass the constrained bandwidth while reserving scientifically valuable data is to prioritize the data onboard. I use the example of UCIS-Moon, an imaging spectrometer with a mission to the south pole of the Moon, to prove the implications of onboard data prioritization. UCIS-Moon extends to 3.6 μm, a spectral region not yet studied extensively at the lunar surface. In order to test onboard prioritization algorithms, I created a dataset extending into this spectral range, based on previously collected lunar orbital and laboratory data. The results of this study will benefit future imaging spectrometers developed for lunar studies and show that the algorithms tested can reduce a returned dataset by at least 29%.

Table of Contents

List of Figures

ix

List of Tables

Chapter 1: Introduction and Topics of Interest

Planetary exploration is driven by the curiosity to understand how our Solar System formed and how life may have come to exist as a result. In this field, we gain knowledge about planetary formation through chemical analysis of planetary surfaces. This type of study is often carried out through remote sensing, where optical instruments observe reflected light of potentially various wavelengths that have interacted with the molecules and minerals at the surface. The scattered and reflected light can yield characteristic information about the composition of the planetary surface with which it interacted. This dissertation will describe two different innovative techniques and their respective analyses for remotely observing planetary surfaces with the intent of understanding the composition of the surface as well as any signs of extant life.

In particular, the projects in this dissertation aim to touch on three of the main aspects of a planetary mission; development of instrumentation, qualifying the potential of a specified instrument to answer particular science questions, and optimizing the return of collected data.

1.1 Remote Raman Spectroscopy

1.1.1 Theory

Raman spectroscopy is a technique that is used to identify and characterize molecular compounds, such as minerals, by observing an inelastic collision of light with matter called the Raman Effect (Raman, 1928). Illumination of a sample with intense monochromatic light gives rise to narrow emission lines due to the Raman Effect that are diagnostic of the molecular composition of the sample (Ferraro et al., 2003). The inelastic collision observed in the Raman Effect describes the exchange of energy between the various vibrational modes in a particular

molecule and an incident light source. Vibrational modes are distinct and depend on bond strength, length, angle, and molecular symmetry (Acosta-Maeda et al. 2016). As the vibrational modes of each molecule are unique, the changes in energy observed via the frequency of the scattered light serve as a spectral fingerprint for each molecule (Sharma & Egan, 2019).

Remote Raman spectroscopy in daylight conditions poses challenges because the Raman effect is weak (about one in ten thousand photons are scattered via the Raman Effect). The system used to collect remotely Raman scattered light must be time-resolved in order to minimize background from sunlight and long-lived fluorescence from transitional-metal ions, rare-earth ions, and particular mineral targets. For this reason, the incident light source used in the system discussed in Chapters 2 and 3 is a pulsed
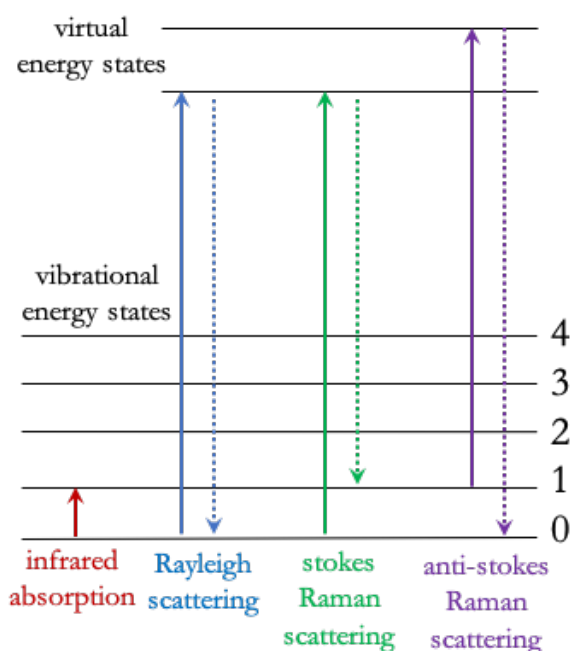
Figure 1.1: A schematic of the quantum energy states used to describe the Raman effect.

laser at 532 nm and the system is equipped with a gated detection system that is adjusted based on sample distance and the speed of light in air. During the brief period of laser illumination, the time-resolved Raman signal is brighter than the continuous sunlight. Thus, each pulse that interacts with a sample and is scattered via the Raman Effect is detected independently and the background is reduced while the long-lived fluorescence is mitigated.

While Raman spectroscopy is a typical laboratory technique, it can also be used remotely over distances of a few to a few hundred meters (e.g. Sharma et al., 2003, 2006, 2012; Misra et al., 2012, 2018, 2020; Gasda et al., 2015; Angel et al., 2012; Sandford et al., 2020 (Chapter 2)). An optical system that is capable of remote Raman spectroscopy is advantageous to a payload since it does not need to be in contact with a sample in order to make a mineral or organic identification. A rover or lander will benefit from this technology in particular as a remote Raman system will extend the reach of these payloads by hundreds of meters.

Figure 1.2: An image of Jupiter's Moon Europa.

1.2 The Surface of Ocean Worlds

Analyses during the past few decades of outer Solar System exploration reveal the potential habitability of Jupiter and Saturn's icy moons. The term "ocean world" describes those icy moons that likely have a liquid water ocean underneath their outer ice shell (i.e. Europa, Ganymede, Calisto, Enceladus, Titan (Hand and German, 2018; Hendrix and Hurford et al., 2019)). The Galileo spacecraft collected many initial measurements of the Jupiter satellites including imaging surface characteristics and the detection of induced magnetic fields that gave rise to the theory that these icy moons foster a liquid ocean underneath the outer icy shell (Kimura et al., 2015). However, this data set is not sufficient to determine habitability. The National Academies of Science conducted a decadal survey of planetary science in 2011, *Vision and Voyages for Planetary*

Science in the Decade 2013–2022, which promotes a flagship mission to explore the potential of ocean worlds in the outer Solar System to host life (Space Studies Board 2011).

Jupiter's moon Europa is of particular interest to the planetary community due to the high probability of a liquid ocean with potential to sustain life. Because of this ocean's potential suitability for life, Europa is one of the most important targets in all of planetary science. The surface composition of Europa and the energy from radiation trapped in Jupiter's intense magnetic field yield a unique environment on Europa's surface where complex molecules can be created and sustained (Trumbo et al., 2019), or broken (Nordheim et al., 2018). Near IR and visible range spectroscopic measurements from Earth observatories and the Galileo spacecraft reveal the presence of some elements, CHNOPS (carbon, hydrogen, nitrogen, oxygen, phosphorus, and sulfur), that are the essential basic elements needed for biosynthesis on the surface of Europa (Pappalardo et al., 2013). Creating and measuring samples with these characteristics is relevant to a potential lander mission to Europa's surface. In particular, using a compact and remote Raman spectrometer to successfully detect relevant samples would promote the idea of such an instrument onboard a payload bound for ocean worlds to explore their habitability.

1.3 Imaging Spectrometer Large Data Sets

Planetary optical instruments with high spectral and spatial resolution collect large data volumes that are problematic for efficient transmission back to Earth. Hyperspectral imaging spectrometers in particular collect dense spectral data cubes that can characterize the presence of various minerals, volatiles, and organics. As
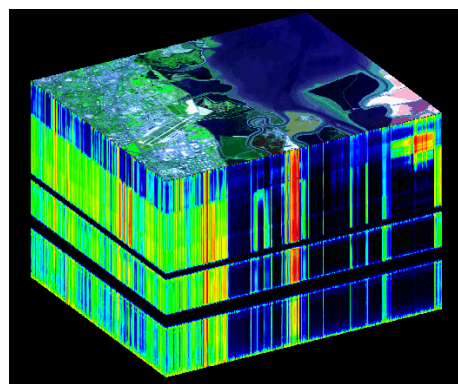
Figure 1.3: An example image cube produced from an imaging spectrometer. Image credit to NASA JPL (AVIRIS).

imaging spectrometers continue to advance, growing data volumes have surpassed the available downlink bandwidths, meaning it is not feasible for all of the data collected by the instrument to be sent back to Earth. Developing onboard processing algorithms that screen data in real time is one solution to this problem. In particular, onboard prioritization (i.e., screening spectral pixels onboard for the presence of absorption features of interest and prioritizing them for return to Earth) can improve the breadth of scientifically relevant returned data, while maintaining high spectral resolution.

Chapter 2: Detecting Minerals and Organics Relevant to Planetary Exploration Using a Compact Portable Remote Raman System at 122 Meters

Abstract Raman spectroscopy is a technique that can detect and characterize a range of molecular compounds such as water, water ice, water bearing minerals and organics of particular interest to planetary science. The detection and characterization of these molecular compounds, which are indications of habitability on planetary bodies, has become an important goal for planetary exploration missions spanning the Solar System. Using a compact portable remote Raman system consisting of a 532 nm Nd-YAG-pulsed laser, a 3-inch diameter mirror lens and a compact spectrograph with a miniature intensified charge coupled device (mini-ICCD), we were able to detect water (H_2O), water ice (H_2O-ice), CO_2-ice, hydrous minerals, organics, nitrates, and an amino acid from a remote distance of 122 m in natural lighting conditions. To the best of our knowledge, this is the longest remote Raman detection using a compact system. The development of this uniquely compact portable remote Raman system is applicable to a range of Solar System exploration missions including stationary landers for ocean worlds and lunar exploration, as they provide unambiguous detection of compounds indicative of life as well as resources necessary for further human exploration.

2.1 Introduction

Raman spectroscopy is a technique that characterizes the spectroscopic result of the inelastic collision between light and matter. This technique identifies molecular compounds by

observing a change in the frequency of scattered light due to the energy exchange between the light and the target's molecular vibrational and rotational modes (Ferraro et al., 2003). The observed change in frequency or wavelength in the scattered light is called the Raman Effect (Raman, 1928). Vibrational modes are unique to each molecule and depend on cation and anion masses, bond strength, length and angle, as well as molecular symmetry (Acosta-Maeda et al., 2016). Thus, the shifts in frequency of the scattered light from the wavelength of the stimulating radiation serve as a spectral fingerprint for each molecule. This technique is widely applicable to a variety of fields including geology and planetary exploration as well as national security and medicine (Griffith et al., 2003; Fini et al., 2003; Petry et al., 2003; Hanlon et al., 2000; Rull Perez et al., 1999; Kiefert and Karampelas, 2011; Moore and Scharff, 2009; Wang et al., 1995; Rull Perez and Martinez-Frias, 2006; Angel et al., 2012; Sharma et al., 2011). In this work, we aim to demonstrate that Raman spectroscopy is a powerful tool for planetary exploration and that a compact portable remote Raman system that can detect molecular compounds at hundreds of meters will be useful for planetary missions spanning the Solar System.

The NASA Decadal Survey (2013-2022) highlights the significance of this work by outlining the importance of the search for life outside of Earth within our Solar System. As stated in the survey, "the processes [from which life originated] likely involve the simultaneous presence of organic compounds, trace elements, water, and sources of energy" (Space Studies Board, 2011). The detection of any or all of these indicators yield important information about whether or not a given planetary body could have hosted or can presently host life. Unambiguous detection of hydrated minerals, molecular water, and the presence of amino acids (the building blocks of proteins) could change how we understand the possibility for life outside of Earth. Raman

spectroscopy is an important tool to unambiguously detect and characterize these compounds (Sharma et al., 2011; Rull et al., 2011; Sharma et al., 2009; Sharma et al., 2006; Misra et al., 2012).

NASA's Mars rover *Curiosity* has used another form of laser induced spectroscopy called Laser Induced Breakdown Spectroscopy (LIBS), which provides information about the elemental composition of the red planet (Wiens et al., 2012). This method is not directly sensitive to the molecular composition of targets and cannot distinguish between molecular phases. This technique also has difficulty in correctly identifying and distinguishing a vast number of organics that include the same elements such as C, H, N, and O. The atmosphere on Mars further complicates the analysis of the signal return from targets since atmospheric CO_2 gas signatures are always present. In order to establish habitability, which relies on inferences regarding the mineralogy and organic biosignatures of ancient environments, we must be able to distinguish one molecular signature from another with a high level of confidence. Raman spectroscopy addresses this concern since the observed shifts in frequency are due to the vibrational modes of molecules and crystal lattices, whose structural symmetry dictates the number of Raman lines seen. Thus, a Raman spectrum serves as a unique "fingerprint" of the target that yields positive identification.

Two upcoming missions to Mars will include Raman spectrometers onboard (Beyssac et al., 2020). NASA's *Perseverance* rover will have both a micro-Raman (SHERLOC; Scanning Habitable Environments with Raman and Luminescence for Organics and Chemicals) and a remote Raman system (SuperCam) to study Martian rocks at Jezero Crater. SuperCam uses a time-resolved intensified spectrograph with 12 cm^{-1} resolution in the spectral range from 536 - 855 nm (Wiens et al., 2012). The spectrograph uses a lens to couple the intensifier to a CCD (charge coupled device) camera to record spectral measurements. ESA's ExoMars *Rosalind Franklin* rover will carry a micro-Raman system (RLS; Raman Laser Spectrometer) to Oxia Planum to study

samples collected using the rover's drill. RLS is comprised of a 532 nm CW (continuous-wave) Nd:YAG laser, with a spectral resolution between 6 and 8 cm^{-1} in the spectral range from 533 – 676 nm (Rull et al., 2017). Both of these systems use volume phase holographic transmission gratings. We aim to use the technology developed through these missions to build Raman systems with more capabilities. The particular system used in this experiment extends the capability remote Raman systems to measure samples at further distances than previously recorded while producing equivalent spectral resolution to SuperCam.

The Raman Spectroscopy laboratory at the University of Hawaiʻi (UH) at Mānoa has previously developed instrumentation for planetary exploration that has had a significant impact on the remote Raman spectroscopy community's development of innovative instruments (Acosta-Maeda et al. 2016; Misra et al., 2012; Sharma et al., 2012; Misra et al., 2020; Gasda et al., 2015; Sharma et al., 2006; Sharma et al., 2003; Angel et al., 2012; Misra et al., 2018). Most recently, we have performed Raman spectroscopy during afternoon natural lighting conditions from 1752 m using an 8-inch diameter telescope as collection optics and with integration times ranging from 1 to 30 s (Misra et al., 2020). Remote Raman spectroscopy in natural lighting conditions poses challenges first due to Raman signals being intrinsically weak (Sharma et al., 2012) and secondly due to the impact of sunlight and long-lived fluorescence, from trace impurities of transition-metal and rare-earth ions in minerals and rocks, which reduces the signal-to-noise ratio of the already low-intensity Raman scattered light (Blacksberg et al., 2016; Misra et al., 2005). A time resolved system including a pulsed laser and a gated detection system addresses these concerns.

In this study, we have evaluated the long-range performance of a custom compact spectrograph equipped with a 3-inch diameter mirror lens and a mini-ICCD camera. We present the detection of molecular compounds relevant to planetary exploration (Table 2.1) such as water,

water-ice, CO_2-ice, water bearing minerals, and organics at 122 m using a compact portable remote Raman spectrometer developed at UH Mānoa.

Table 2.1: Samples measured and the relevance of these samples to planetary exploration with associated literature references.

Type	Samples	Planetary Astrobiological Significance	Relevance Cited in Literature
Water & Frozen Compounds	Liquid H_2O	Moon, Mars, Ocean Worlds	NASA Astrobiology Strategy (2015)
	H_2O Ice	Moon, Mars, Ocean Worlds	NASA Astrobiology Strategy (2015)
	CO_2 Ice	Mars, Ocean Worlds	NASA Astrobiology Strategy (2015)
Hydrous Minerals	Gypsum	Mars, Ocean Worlds	Horgan et al. (2009); Martinez-Frias et al. (2006)
	Epsomite	Mars, Europa, Ocean Worlds	Dalton III et al. (2012); Martinez-Frias et al. (2006)
Organic Compounds	Urea	Asteroids, Interstellar Media, Ocean Worlds	Brigiano et al. (2018)
	Naphthalene	Asteroids, Interstellar Media, Ocean Worlds	Parker et al. (2012)
	Nitrobenzene	Asteroids, Titan, Ocean Worlds	Abbas and Schulze-Makuch (2002)
Nitrates	Potassium Nitrate	Mars	Stern et al. (2015); NASA Astrobiology Strategy (2015)
	Ammonium Nitrate	Mars	Stern et al. (2015); NASA Astrobiology Strategy (2015)
Amino Acid	β-Alanine	Asteroids, Europa, Ocean Worlds	NASA Astrobiology Strategy (2015)

2.2 Experimental Methods

The unique remote Raman system developed at UH for this study and the samples that were measured are described below. The measurements for this work were collected in a 128 m outdoor hallway on the UH Mānoa campus. The Raman system is mounted on a trolley for use in

either a laboratory or outdoor setting. In this experiment, the natural lighting conditions described are measured as solar irradiance, averaging to 151 W/m^2 in the month of December, when the measurements were collected (Giambelluca et al., 2014). The target samples were placed at one end of the hallway and the detection system was placed at the opposite end of the hallway (Figure 1), yielding a sample-to-system distance of 122 m. The remote Raman system is a time-gated system where measurements of a distant target located at an unknown distance can be performed by taking time-series measurements with a system delay. For example, starting at 0 ns and ending at 10,000 ns with a gate width of 100 ns will provide a sampling depth of 15 m with a target located at 1500 m. An example of a time series Raman measurement of atmosphere and a target at 1752 m is shown in Figure 3 of Misra et al. (2020) and shows a distinguished Raman signal at the corresponding time compared to the background.
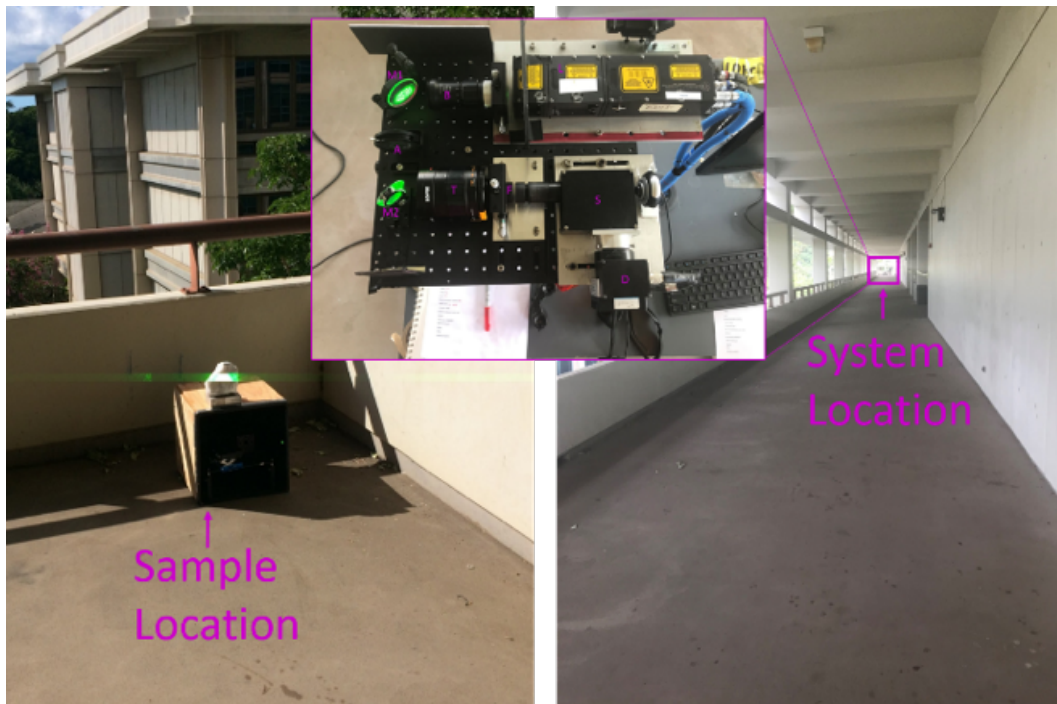
Figure 2.1: The experimental set up including the target sample location (left), the Raman system location (right), and an aerial view of the Raman system (top center).

2.2.1 The Raman System

The compact portable remote Raman system consists of several components (Figure 2.2). The excitation source is a 532 nm Nd:YAG pulsed laser, at 20 Hz and 20 mJ/pulse (Model Ultra CFR, Big Sky Laser Technologies). The laser is triggered using an external triggering pulse-delay generator (Model 575, Berkeley Nucleonic Corporation). As the measurements are time-resolved, the triggering system first initializes the diode and Q-switch in the laser, then uses these triggers to initiate the intensified CCD (ICCD) camera. The system is arranged in a coaxial geometry where the laser beam, expanded from a compact 10 x beam expander, is aligned with the optical axis of the mirror lens, spectrograph, and mini-ICCD through two folding mirrors before being sent towards the target sample. The spot size at the sample in this experiment was approximately 10 mm in diameter. A 25 mm diameter catadioptric mirror lens (Bower Optical) collects the scattered light from the target sample and passes it through a 532 nm notch filter before focusing the light onto a 50 µm slit to pass to the mini-ICCD camera through the spectrograph. We take advantage of the lens central obscuration to re-route the output beam using a fold mirror that creates a truly colinear system. The compact spectrograph (10 cm (length) x 8.2 cm (width) x 5.2 cm (height)) consists of a custom Holoplex grating from Kaiser Optical Systems Inc., which splits the spectral range (100 - 4200 cm^{-1}) into two traces on the mini-ICCD camera, from Syntronics, Fredericksburg, VA. In particular, the mini-ICCD camera uses a fiber-optic rather than a lens system to couple the image converter phosphor to the CCD array. The fiber-optic coupling is at least 2.5 times more efficient than a F/2-lens coupled design (Sharma et al., 2012). The fiber-optic coupling of the ICCD chip also makes the detector compact and lightweight. This spectrograph has a spectral resolution of 12 cm^{-1}. The entire Raman system is mounted on a pan and tilt plate

for alignment with samples at large distances. The optimal delay time was determined by taking a series of Raman spectra using a fixed gate of 70 ns and varying the delay time. The delay time at which the Raman spectrum of the sample showed the maximum intensity was selected for making measurements. This technique works well for optimizing the spectrum of samples at an unknown distance from the standoff Raman system (Wiens et al., 2017).
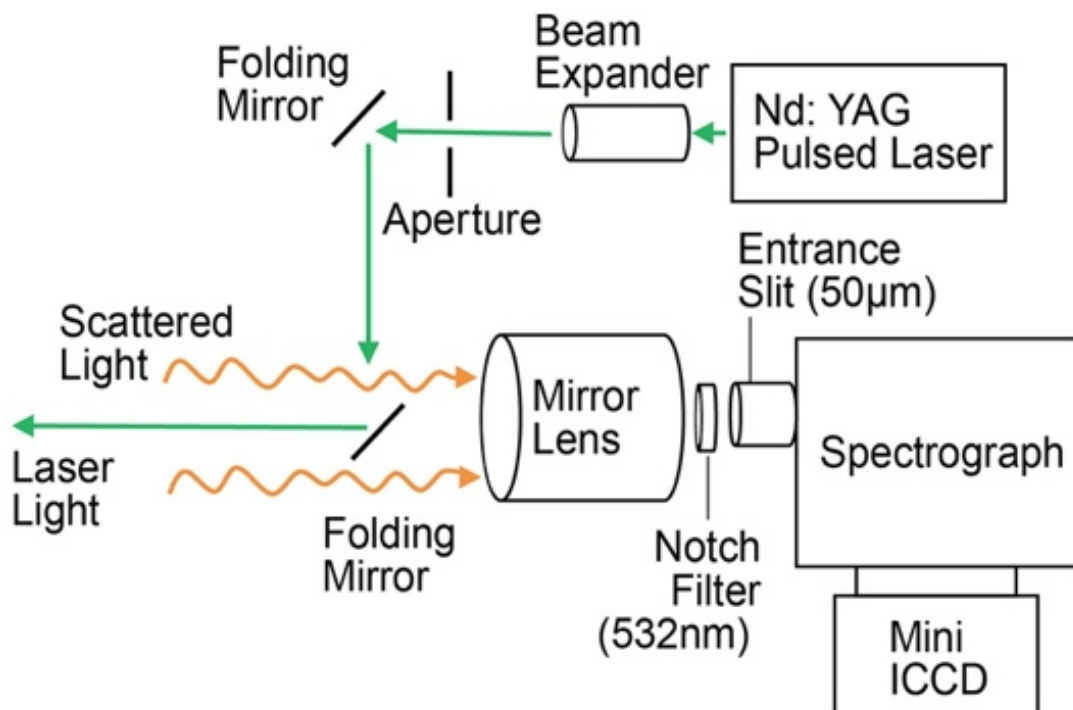
Figure 2.2: A block diagram of the Raman detection system used to collect Raman spectra.

2.2.2 Samples and Processing of Spectra

Rock and mineral samples were obtained from Ward's Natural Science Establishment, Inc., Rochester, New York. These samples were not cut or polished after being received. We obtained the amino acids from Sigma Aldrich and placed them in 20 ml glass vials for measurement. Liquid chemicals (ACS grade) were obtained from Fisher Scientific and portioned into glass containers for measurement. Potassium nitrate, ammonium nitrate, and urea were obtained from Fisher Scientific. Tap water from the city of Honolulu, Hawaiʻi was used for both liquid H_2O and H_2O-

ice samples. Dry ice (CO_2-ice) was locally obtained in the form of pellets. The spectra of samples presented in this study were collected with 30 seconds integration time, which amounts to 10 laser pulses and 60 camera accumulations with our system. The timing of the mini-ICCD camera gate, which is delayed from the Q-switch, changes depending on the distance between the system and the target sample in order to adjust for the time it takes the laser pulse to reach the target sample and the resulting scattered light to reach the detector. Obviously, at longer distances the ICCD camera gate is delayed longer in order to synchronize with the arrival of the Raman photons. The mini-ICCD is operated with a short gate width (70 ns) to mitigate background light from overwhelming the Raman signal and allows for longer range detection outdoors in natural lighting conditions. The features seen in all spectra around 1555 cm^{-1} and 2331 cm^{-1} are due to atmospheric O_2 and N_2, respectively.

Spectra are derived from taking cross-sections of the images projected on the mini-ICCD camera through the spectrograph. The software used to collect images from the mini-ICCD camera is a customized software built to operate with the camera. We stitched the resulting spectra from each trace together using GRAMS/32 software package from Galactic Industries Corporation. We used custom MATLAB software called "Raman1" developed at UH to calibrate the data. The Raman spectra were calibrated using the known Raman spectral peaks of calcium carbonate, cyclohexane, sulfur, atmospheric nitrogen, acetonitrile, and the R_1 and R_2 luminescence lines of a ruby (Al_2O_3 doped with Cr^{3+}).

2.3 Results and Discussion

Using the system described above, a compact portable remote Raman system incorporating highly efficient direct optical coupling (Misra et al., 2005), we successfully obtained Raman peaks

of relevant hydrous compounds and minerals, organic compounds, nitrates, and an amino acid at

122 m distance in natural lighting throughout the day with an integration time of 30 s (Table 2.1).

Specifically, the 30 s integration time was comprised of 10 laser pulses per camera accumulation

and 60 total accumulations. The 532 nm laser used was set to a 20 Hz pulse rate, 8 ns pulse width

at full width half max, and energy of 20 mJ/pulse. The ICCD was set to a gated delay of 813 ns

and a gate width of 70 ns. Each measurement has a signal-to-noise ratio (SNR) above 3, which is

the standard for detection (Table 2.2). The SNR calculation used for the values in this table is

described in McCreery (2000). Simply, $SNR = \bar{S}/\sigma_S$, where $\bar{S}$ is the mean intensity of the three

measurements collected at the strongest peak in the spectrum and σ_s is the standard deviation of

the intensity of the three measurements. It is evident from Table 2.2 that the calculated SNR values

vary depending on the respective Raman cross-sections for these materials.

Table 2.2: The signal-to-noise ratio (SNR) for each measurement calculated using the mean and standard deviation of three measurements (McCreery et al., 2000).

Samples	Strongest Peak Position (cm^{-1})	Mean	Standard Deviation	Signal-to-Noise Ratio (SNR)
Liquid H_2O	3442	495534.20	13569.90	51.64
H_2O Ice	3149	426697.91	4538.41	132.96
CO_2 Ice	1392	753367.88	30222.13	35.25
Gypsum	1007	2238412.08	33185.26	95.39
Epsomite	983	2007962.58	85059.97	33.38
Urea	1011	1203405.38	109772.74	15.50
Naphthalene	1380	900806.90	18779.22	67.84
Nitrobenzene	1347	7781075.33	65552.55	167.87
Potassium Nitrate	1048	2782341.25	141897.25	27.73
Ammonium Nitrate	1043	4554194.33	115601.09	55.71
β-Alanine	2800	172790.43	18285.53	13.36

The measurements of liquid H_2O, H_2O-ice and CO_2-ice are compiled and displayed with their characteristic Raman peaks (Figure 3). The water molecule (H_2O) yields a strong, broad signal in the 3000-3600 cm^{-1} spectral region, making it ideal for detection. The broad H_2O feature is due to the symmetric (v_1) and antisymmetric (v_1) stretching vibrational modes of the O-H stretching modes of the water molecule. The solid phase of water (H_2O-ice) is distinguished from liquid water in Raman spectra from the sharp band, around 3149 cm^{-1}, found within the characteristic broad O-H signal (Figure 3) This sharpened feature in the H-O-H symmetric stretching mode (v_1) comes from the increased ordering in the H_2O ice structure (Oh et al., 2015). The strengthening of the hydrogen bonds as water changes from liquid to ice causes a shift of the feature to lower frequencies (Myneni et al., 2002; Whalley et al., 1977). The two strong features seen in the CO_2-ice spectrum at 1275 cm^{-1} and 1385 cm^{-1} are due to a Fermi resonance of the active symmetric stretching (v_1) vibrational mode of the isolated CO_2 molecule and the overtone of the IR active bending mode ($2v_2$) of the molecule. The resulting features are called a Fermi doublet (Sharma et al., 2012).
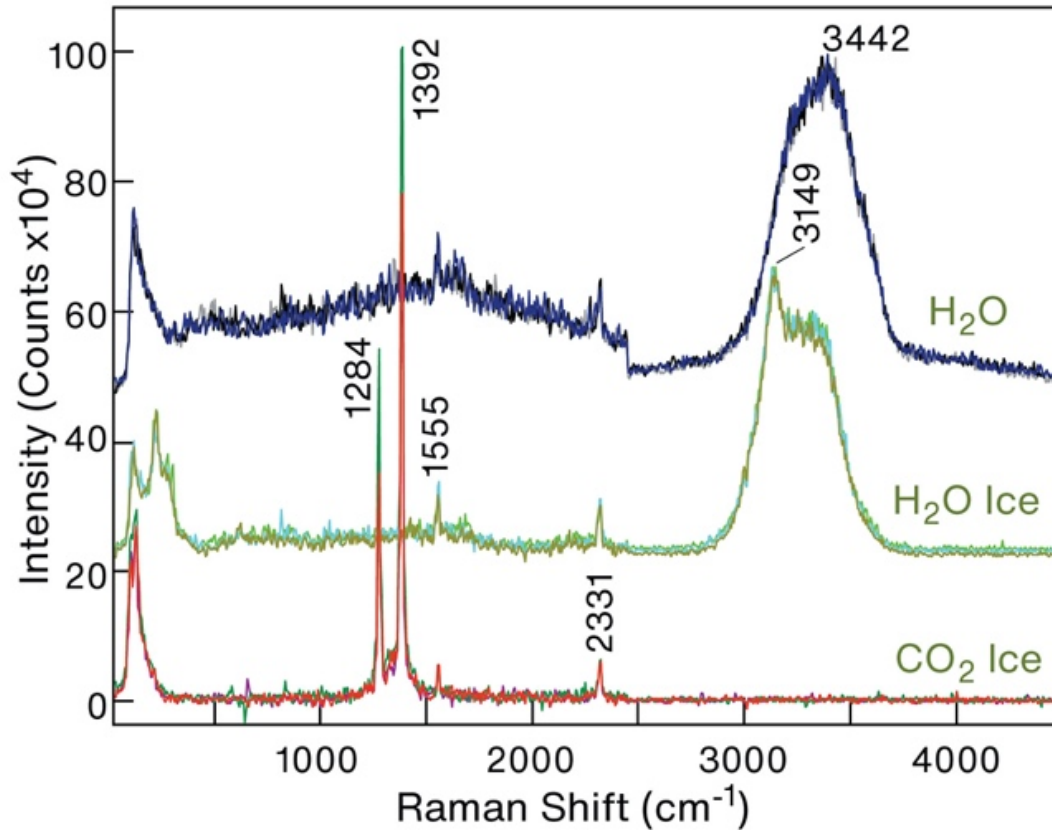
Figure 2.3: Raman spectra of liquid H2O, H2O-ice and CO2-ice collected using the described system at 122 meters during natural lighting hours with a 30 s integration time.

Raman peaks of the hydrous minerals gypsum ($CaSO_4.7H_2O$) and epsomite ($MgSO_4.7H_2O$) were successfully detected and the resulting spectra are compiled in Figure 2.4. The sulfate anion in both minerals gives a strong Raman band near 1000 cm^{-1}. The symmetric stretching vibrations (v_1) in the sulfate ions (SO_4) are observed at 1007 cm^{-1} in gypsum and at 983 cm^{-1} in epsomite. The position of the sulfate band can also determine the hydration state of the chemical (Wang et al., 2006). The chemically bonded water molecules in gypsum are observed at 3405 cm^{-1} and 3491 cm^{-1} and distinguish this mineral from epsomite, which has a much broader O-H stretching feature in the high frequency range (McKinnon and Zolensky et al., 2003).

17
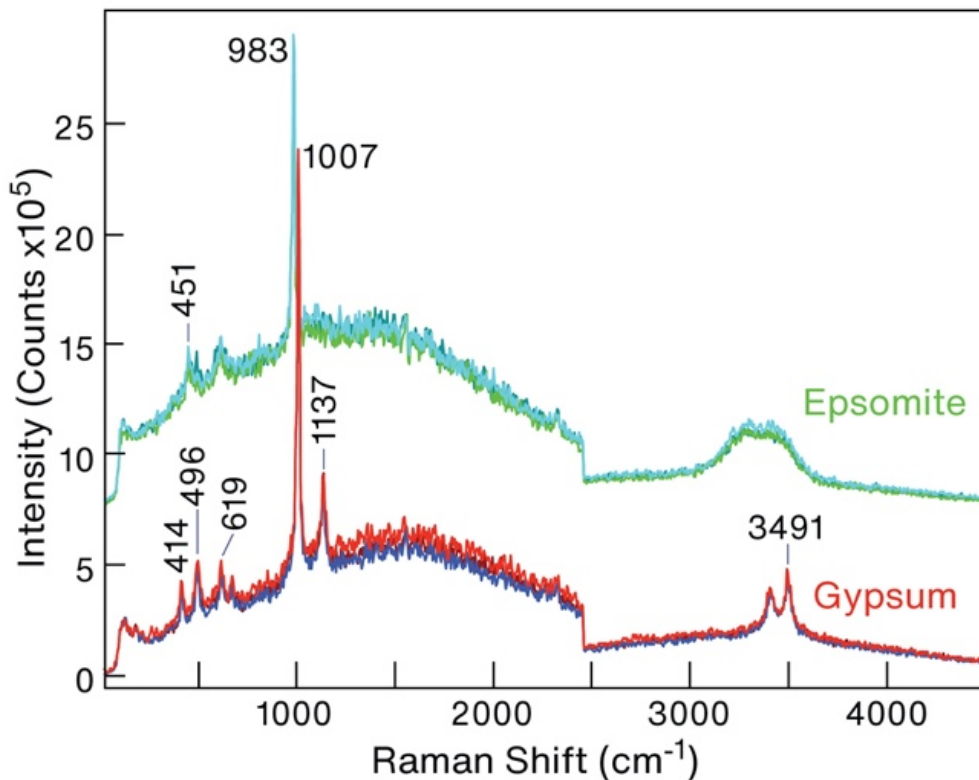
Figure 2.4: Raman spectra of epsomite (MgSO4•7H2O) and gypsum (CaSO4•2H2O) collected using the described system at 122 meters. Experimental conditions were the same as Figure 2.3.

Organics urea, naphthalene, and nitrobenzene were detected at 122 m in natural lighting conditions with a 30 s integration time (Figure 2.5). Seen in the urea spectrum is the distinct peak at 1009 cm^{-1} that corresponds to the NCN symmetric stretch mode of the urea molecule (Culka et al., 2010; Frost et al., 2000). The peak at 1553 cm^{-1} corresponds to the NH_2 bending mode. The stretching modes of the C-O group, free and hydrogen-bonded, produce peaks at 1574 cm^{-1} and 1643 cm^{-1} (Acosta-Maeda et al., 2016).

Naphthalene ($C_{10}H_8$) is shown in Figure 2.5 with the most intense peak at 1380 cm^{-1}, due to the symmetric stretch vibration (v_1) of the symmetric stretching mode of the double ring of the molecule. There are also nine other symmetric stretching modes in the naphthalene molecule seen

18

at 514, 763, 1021, 1462, 1575, 3056 cm^{-1}. Most significantly, the 3056 cm^{-1} line corresponds to the aromatic C-H symmetric stretching mode (Lippincott et al., 1955).

The nitrobenzene (C$_6$H$_5$NO$_2$) molecule includes a NO$_2$ functional group, whose Raman active symmetric stretching (ν_1) vibration can be seen in Figure 2.5 at 1347 cm^{-1}. This is the most intense peak in the nitrobenzene spectrum. The less intense peaks are attributed in part to the NO$_2$ functional group's bending vibration (852 cm^{-1}), the aromatic ring bending (1004 cm^{-1}), the C-N stretching (1108 cm^{-1}) and aromatic ring stretching (1587 cm^{-1}) (Misra et al., 2012).
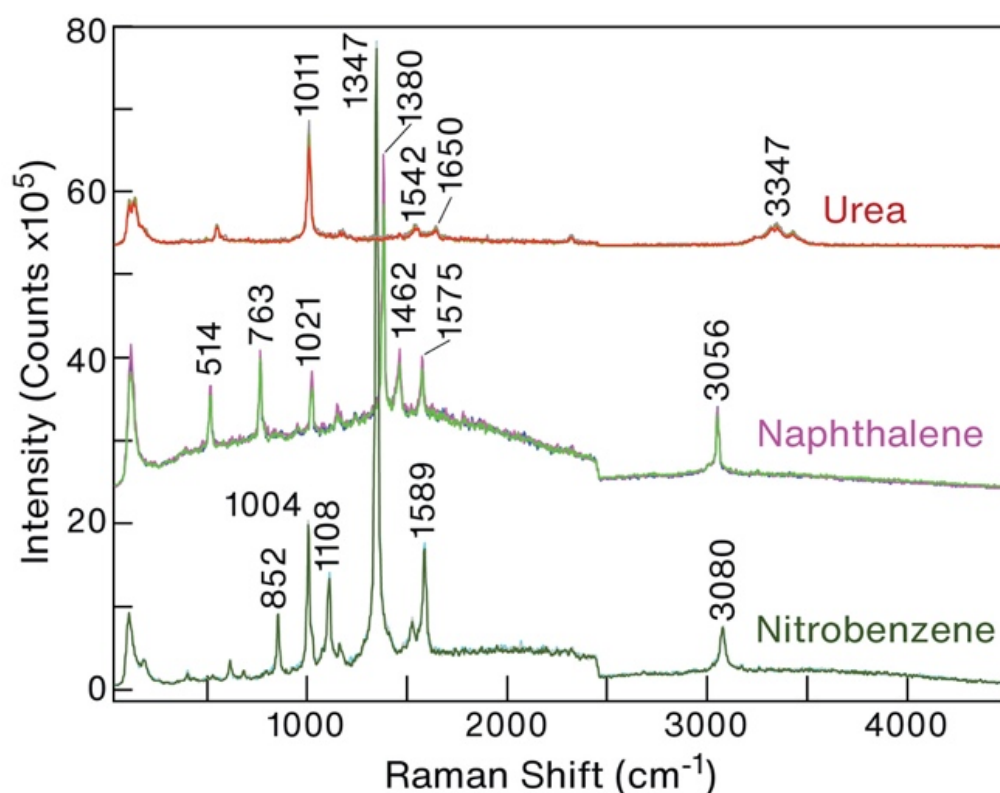
Figure 2.5 Raman spectra of Urea (CO(NH2)2), Naphthalene (C10H8), and Nitrobenzene (C6H5NO2) collected using the described system at 122 meters. Experimental conditions were the same as Figure 2.3.

The spectra of potassium and ammonium nitrate were collected from 122 m in natural lighting conditions with a 30 s integration time (Figure 2.6.). The NO$_3^-$ ion in the potassium nitrate (KNO$_3$) molecule has a symmetric stretch (ν_1) vibration seen at 1048 cm^{-1} (Figure 2.6.). Ammonium nitrate

(NH4NO3), shown in the same figure, also has an intense Raman peak due to the symmetric stretch of the same ion, located at 1041 cm^{-1}. The peak seen at 715 cm^{-1} in both nitrates is due to the in-plane bending (v_4) vibration of the NO_3^- ion. There is a noticeable difference in the ammonium nitrate spectrum that easily differentiates it from the potassium nitrate spectrum seen in the high-frequency region near 3100 cm^{-1}. This feature is attributed to the symmetric stretch (v_1) vibration of the NH_4^+ ion in ammonium nitrate. The broad feature is also in part due to the asymmetric stretching mode found near 3225 cm^{-1} (Misra et al., 2012).
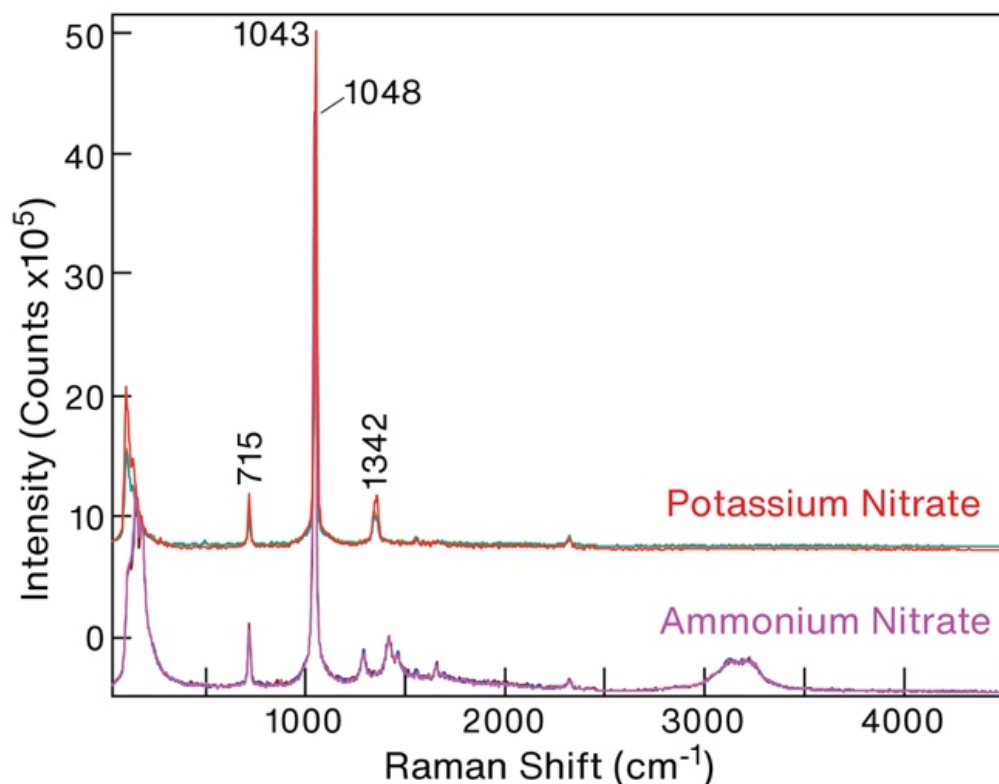
Figure 2.6: **Raman spectra of Potassium Nitrate (KNO3) and Ammonium Nitrate (NH4NO3) collected using the described system at 122 meters. Experimental conditions were the same as Figure 2.3.**

The amino acid β-Alanine (β-$C_3H_7NO_2$) (98% purity) was detected at 122 m and the resulting spectrum is presented in Figure 2.7. Amino acids are important to detect since they indicate the presence of proteins. Raman bands in the CH stretching region (2800-3100 cm^{-1}) indicate the

presence of the β-Alanine amino acid (Acosta-Maeda et al, 2018). The COO- symmetric stretching vibration is seen at 1390 cm^{-1} while the C-N stretching vibration is located at 1061 cm^{-1}. The intense peaks seen at 940 cm^{-1} and 848 cm^{-1} are due to the CH$_2$ rocking vibration and C-CN stretching vibration (Culka et al., 2010), respectively. We have previously reported remote Raman spectra of various amino acids and DNA (deoxyribonucleic acid) bases using this system from a 10 m distance (Acosta-Maeda et al, 2018).
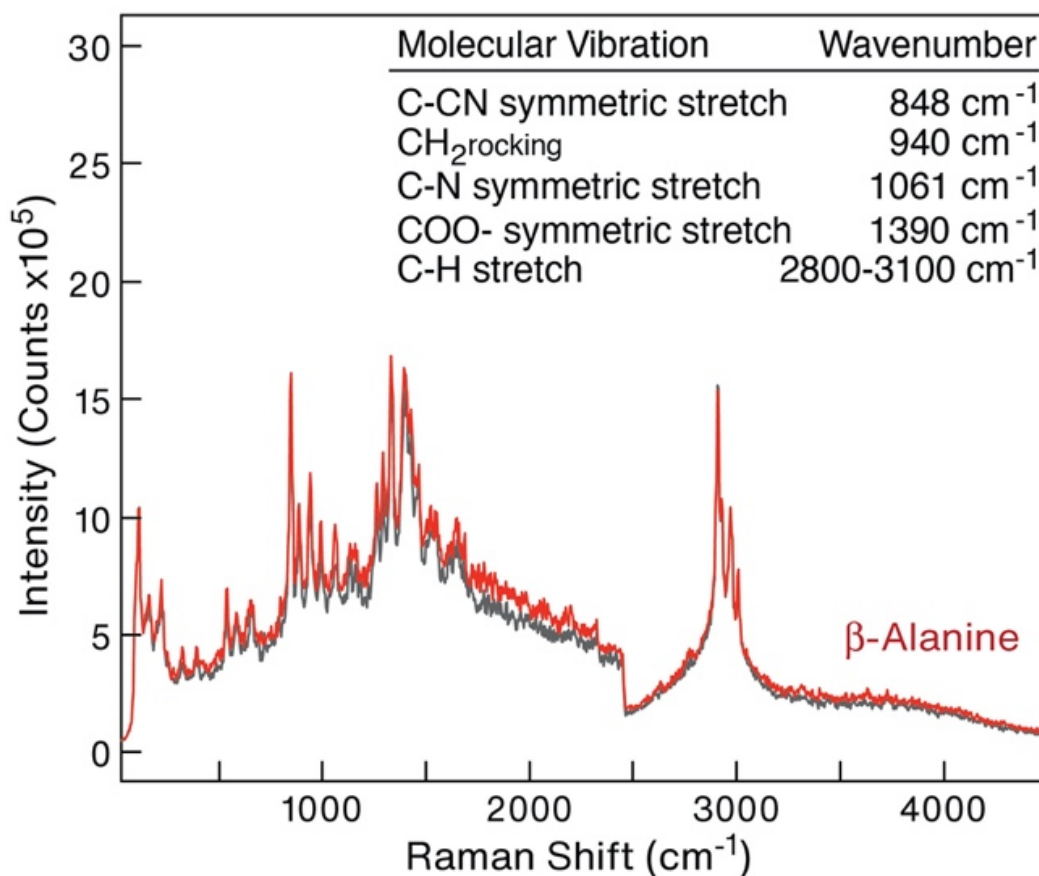
Figure 2.7: Raman spectrum of the amino-acid β-Alanine (β-C3H7NO2) collected using the described system at 122 meters. Experimental conditions were the same as Figure 2.3.

2.4 Conclusion

We successfully detected minerals and organic compounds relevant to the search for life in the Solar System using a compact portable remote Raman spectrometer from 122 m during natural

lighting conditions. Remote Raman spectral detections of hydrous compounds, hydrous minerals, organic compounds, nitrates, and an amino acid are presented in this paper. This work is important because Raman spectroscopy is a unique tool that provides unambiguous detection of molecules essential for life as we understand it. Remote Raman spectroscopy in particular harbors the capability to explore potentially habitable worlds in ways not yet presented through other techniques. A compact remote Raman spectrometer such as the one presented in this paper will also drastically increase the range of detection for landers or other planetary explorers on the surface and subsurface of planetary bodies.

Chapter 3: Exploring Ocean Worlds Using a Compact Standoff Raman Spectrometer

Abstract The search for past and present life has led to the water-rich satellites of the outer Solar System. Geologically active icy worlds orbiting Jupiter and Saturn possess global liquid water oceans up to hundreds of kilometers deep, covered by icy shells up to tens-of-kilometers thick. Life may exist at the interfaces of the outer, icy shells and oceans of these worlds. Whether the components needed for life are present in their icy shells or in their subsurface oceans is still unknown, but planetary missions are being developed to answer these questions. The implications of detecting these components carry great significance for how we currently understand the processes that dictate the emergence and proliferation of life. Raman spectroscopy is a uniquely valuable technique in the search for life for several reasons, including the ability to penetrate centimeters into ice, detect organic and inorganic compounds, and actively provide a light source, which is critical at great distances from the Sun. In particular, *remote* Raman spectroscopy is an exciting technique for future missions to study ocean world habitability and potential signs of life because it could extend the reach of a lander, rover, or subsurface probe at the surface of a body by hundreds of meters. In this study, we simulated the surface, icy shell, and ocean of ocean worlds to demonstrate remote Raman spectroscopy as a valuable tool for planetary missions to these bodies. We successfully measured simulant radiation products, salt brines, amino acids, and organics related to the chemistry of ocean worlds with intent to relate these measurments to planetary missions whose purpose is to gain insight into their habitability and potential for past or present inhabitation.

3.1 Introduction

Over the past few decades, planetary scientists have analyzed the satellites in the outer Solar System and have discovered the potential habitability of Jupiter and Saturn's icy moons. Through these analyses, the term "ocean world" was created to describe some of these icy moons that likely have a liquid water ocean underneath their outer ice shell (e.g. Europa, Ganymede, Calisto, Enceladus, Titan (Hendrix and Hurford et al., 2018; Hand and German, 2018)). The Galileo spacecraft investigated the Jovian satellites using imagery to map geologic characteristics, limited spectral instruments to detect and reveal surface composition and texture (Geissler et al., 1998), and magnetometry to investigate permanent and induced fields. The discovery of an induced magnetic field at Europa gave rise to the theory that this icy moon was home to a subsurface liquid ocean underneath its outer, icy shell (e.g. Kivelson et al., 2002; Kimura et al., 2015) (Figure 3.1). However, the present data are not sufficient to determine the habitability of these moons. The National Academies of Science conducted a decadal survey of planetary science in 2011, Vision and Voyages for Planetary Science in the Decade 2013–2022, which promotes a flagship mission to explore the potential of ocean worlds in the outer Solar System to host life (Space Studies Board 2011). As such, NASA's Europa clipper mission (expected launch no later than 2025) (Howell and Pappalardo, 2020) will fly by Europa to investigate its habitability, while ESA's JUICE mission (Grasset et al., 2013) will investigate the comparative habitability of the Jovian ocean worlds, focusing on Ganymede. However, a conclusive discovery of life on an ocean world will require an *in-situ* investigation of the ice shell and ocean (Pappalardo et al., 2013; Hendrix and Hurford et al., 2018).
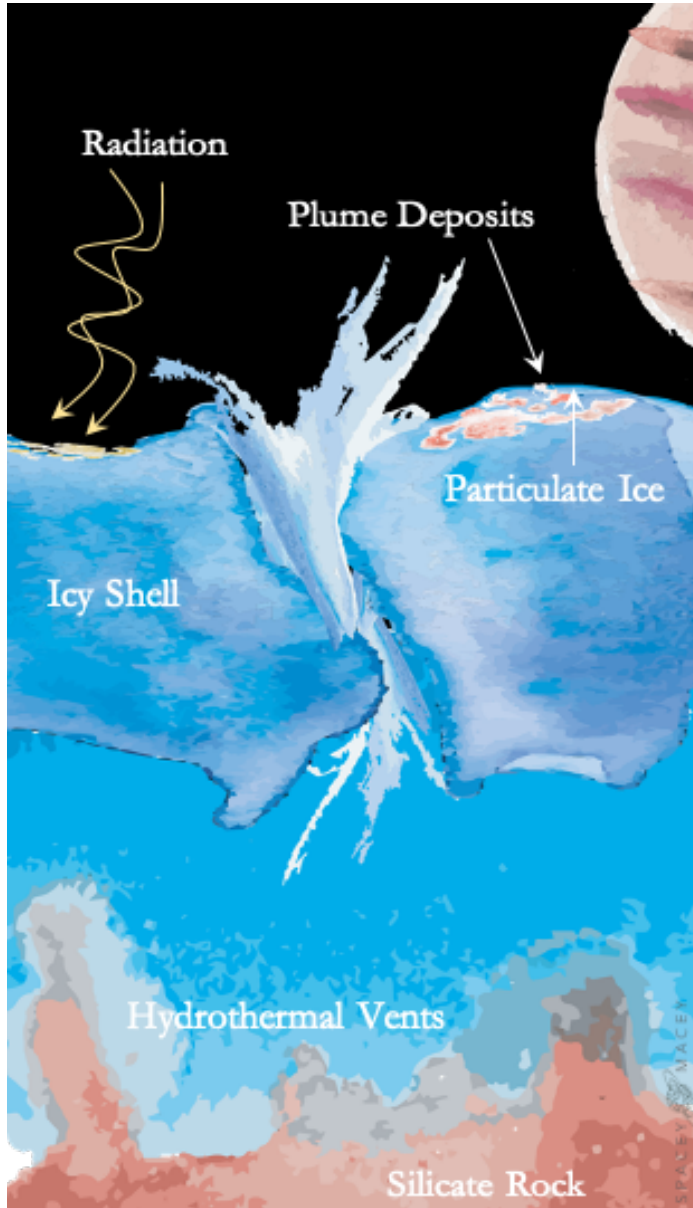
Figure 3.1: A graphic depicting the cross-section of an ocean world. The layers seen in this graphic support the relevance of the solutions created and measured in this study.

The surface composition of Europa is dominated by water ice, and includes salts, some of which originating in the ocean, material deposited from Io and the Jovian plasma, and biogenic material brought from cometary impacts (Carlson et al., 1996; McCord et al., 2010; Vu et al., 2016; Pierazzo et al., 2002). The energy from radiation trapped in Jupiter's intense magnetic field renders a unique environment on Europa's surface where complex molecules can be created and sustained from constituents (Trumbo et al., 2019), or broken (Nordheim et al. 2018). Below the uppermost surface is an icy shell of unknown thickness that may preserve radiation products created at the surface above and/or products created in the liquid ocean below (Korablev et al., 2010; Sephton et al., 2018).

Previous studies of Enceladus and Europa indicate the possibility of plume deposits on the surface originating from the interior ocean (Europa: Jia et al., 2018; Quick et al., 2013; Roth et al., 2014; Paganini et al., 2020; Sephton et al., 2018; Enceladus: Postberg et al., 2018), yielding

information about the chemistry of the interior of these ocean worlds. Creating and characterizing the spectral response of samples similar to those expected from plume deposits on ocean worlds is therefore relevant to a potential landed mission (Pappalardo et al., 2013; Hand et al., 2017). Similarly, samples with characteristics similar to the solid ice shell and liquid ocean are also applicable to future ocean world missions that propose to penetrate the surface and explore the ice shell and ocean-ice interface. We present an analysis of ocean world simulant samples such as frozen and liquid brines, hydrous minerals, and icy organic and amino acid solutions with our Raman system. The specificity and simplicity of Raman and fluorescence spectroscopy make them ideal techniques for ocean world exploration.

Raman and fluorescence spectroscopy provide unique capabilities for detection and characterization of materials of high astrobiological potential, including organic compounds and minerals that may host biosignatures. Further, Raman spectroscopy provides high confidence in the detection of specific molecules based on their intrinsic Raman-active vibrational modes (Ferraro et al., 2003). Previous studies of icy targets with organic and inorganic properties highlight the applicability of Raman spectroscopy to the exploration of ocean worlds (Böttger et al., 2017; Sharma et al., 2019), but we aim to show that detection of relevant ocean world samples using a compact portable remote Raman spectrometer system is far more relevant for a mission to Europa. At the University of Hawai'i at Mānoa (UH), we develop integrated Raman and fluorescence instruments (Figure 3.2) that measure samples remotely. Our instrument has produced high quality Raman spectra at hundreds of meters range for a wide variety of compounds (Misra et al., 2020; Sandford et al., 2020).
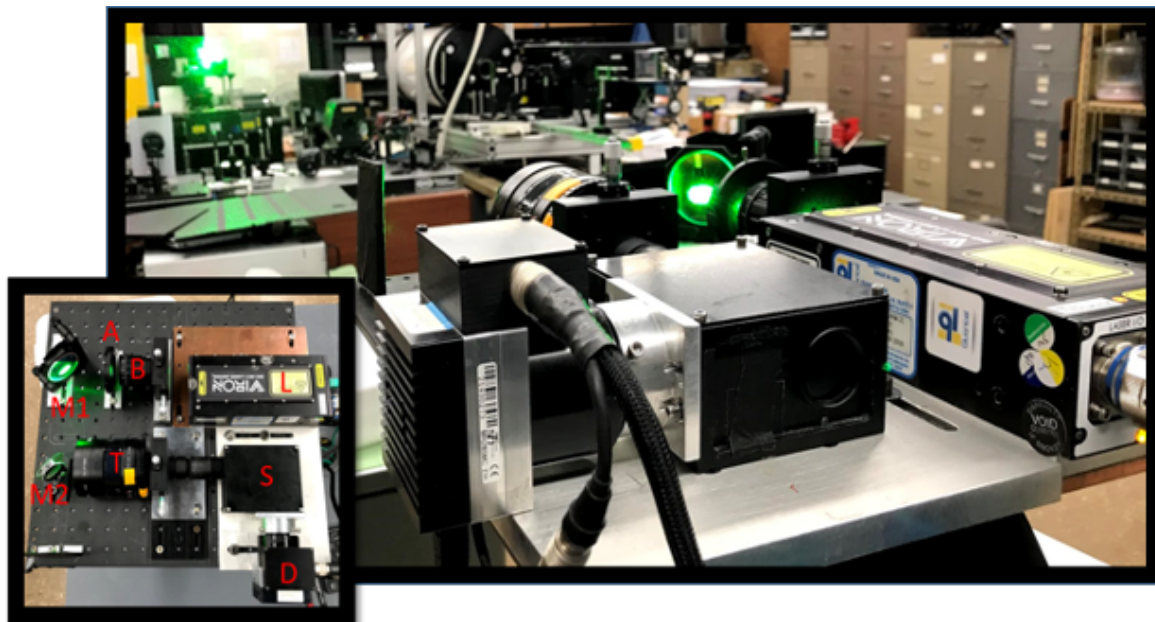
Figure 3.2: Combined compact remote Raman and fluorescence system developed at the University of Hawaiʻi at Mānoa. The system consists of the following; L: Nd:YAG pulsed laser 532 nm, B: 8x beam expander, A: aperture, M1: folding mirror, M2: folding mirror, T: 3" diameter telescope, S: compact Raman/ fluorescence spectrograph, D: mini-ICCD detector, mounted on a Pan and Tilt scanner.

As an ocean world lander or other *in situ* explorer destined for the outer Solar System will have limited mass, volume, and power, we explore using a compact Raman and fluorescence system that operates at low power at a more modest range of 5-10 meters, sufficient to extend the range of static explorers beyond the reach of many robot arms. With this system we are able to routinely measure quantities of pure liquids in the nanoliter range, and minerals in the cubic millimeter range. Substances such as water, amino acids, organics, sulfates, nitrates, oxides, hydrous minerals and several other molecules indicative of life are Raman active and are conclusively identifiable with the remote Raman systems that we have built (Acosta-Maeda et al., 2016; Abedin et al., 2018; Gasda et al., 2015; Misra et al., 2012). We demonstrate the value of a low energy remote Raman spectrometer for the in situ exploration of ocean worlds by measuring

ocean world-relevant salts, brines, phases of water, radiation products, and amino acid solutions with the compact remote Raman spectrometer shown in Figure 3.2.

3.2 Methods

3.2.1 Compact Raman Spectrometer

The optical system used in this experiment consists of a frequency-doubled mini Nd:YAG pulsed laser source (532 nm, 8 ns pulse width, maximum 12.5 mJ/pulse, 20 Hz), two folding-mirrors that provide a colinear geometry, a 3 inch diameter catadioptric mirror lens (Bower Optical), a compact spectrograph (with a 50 µm slit) with dimensions 10 cm (length) x 8.2 cm (width) x 5.2 cm (height) and a mini-ICCD (intensified charge coupled device) camera (Figure 3.2). The laser and collection optics are triggered using an external triggering pulse-delay generator (Model 575, Berkeley Nucleonic Corporation). Further details have been previously discussed in Sandford et al. (2020). The spectra in this experiment were collected in laboratory conditions with all indoor lights turned on (Figure 3.3). Due to the nature of this time-resolved system, background light is mitigated in the resulting spectra since the camera aperture is timed based on the laser's Q-switch and the distance to the target. Samples were measured at a distance of 5 m using the intensified CCD in gated mode with a 40 ns gate width. A short gate width helps in minimizing the background signal from long lived luminescence and the room lights.

Figure 3.3: A compilation of images showing the experimental setup. On the left is a zoomed in image of a sample being measured. On the right is an example of the ICCD image output when measuring a target.

3.2.2 Ocean World Simulant Solutions

We demonstrate the value of remote Raman spectroscopy for the exploration of ocean worlds by measuring samples that characterize the chemistry of these worlds from their surface to their ocean. Our ocean world relevant sample catalog includes particulate ices, solid blocks of ice, and liquids (Table 3.1) (Figure 3.4). Glycine, beta-alanine and sulfuric acid were purchased from Sigma Aldrich. Epsom salt ($MgSO_4 \cdot 7H_2O$) was purchased from a grocery store and was labeled as containing 100% magnesium sulfate USP (heptahydrate). Higher grade hydrated magnesium sulfate salt ($MgSO_4 \cdot 7H_2O$) and anhydrous magnesium sulfate salt ($MgSO_4$) were purchased from Ward Scientific along with the pure gypsum rock sample. The iodized table salt (NaCl) used in the solutions was also bought from the grocery store. Hydrogen peroxide was purchased from the grocery store and contained a 3% concentration of H_2O_2 in liquid-H_2O. Naphthalene, nitrobenzene (ACS grade), and methanol were purchased from Fisher Scientific. Distilled H_2O from the UH chemistry stock room was used as the solvent for preparing the solutions. Liquid samples were

made by dissolving the solutes in the solvent. Particulate ice was created using a Paasche VL#3

airbrush with a 0.75 mm head to spray droplets of the liquid solutions into liquid nitrogen (LN$_2$).

Solid ice was created by pouring liquid solutions into liquid nitrogen. The LN$_2$ used in this process

was from the UH chemistry stock room.
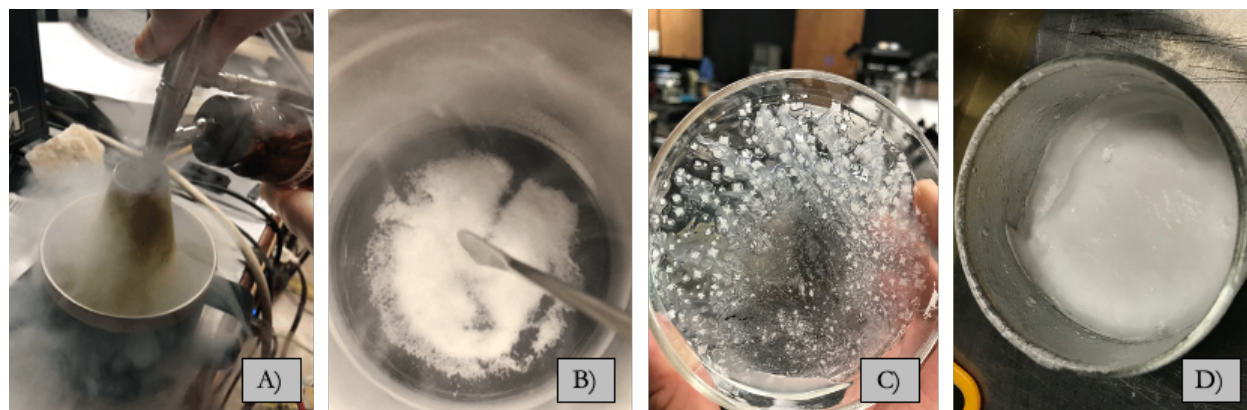
Figure 3.4: Example images of some of the simulant samples; a) Creation of particulate ice using an airbrush and liquid nitrogen, b) particulate ice, c) crystalized brines from melting and evaporation of particulate ice solutions, d) solid ice.

Table 3.1: The solutions successfully measured using a compact remote Raman spectrometer in this experiment with corresponding phase relevant to oceans, solution, and concentration.

Type	Solution	Concentration	Literature Reference
Particulate Ice	Methanol (CH$_3$OH)	32% in H$_2$O	Hodyss et al. 2009
	Hydrogen Peroxide (H$_2$O$_2$)	3% in H$_2$O	Carlson et al. 1999
	Sulfuric Acid (H$_2$SO$_4$)	1 M	Carlson et al. 2002 & Dalton II et al. 2013
	NaCl & MgSO$_4$	1 M	Vu et al. 2016
	NaCl & MgSO$_4$	3.07/1.44 M	Vu et al. 2016
	Glycine	2.46 M	Pappaldaro et al. 2013
	Beta-Alanine	2.46 M	Pappaldaro et al. 2013
	Distilled H$_2$O over Gypsum	Pure	
	Distilled H$_2$O	100%	NASA Astrobiology Strategy (2015)
	Crystallized Brine	Unknown	Carlson et al. 2009
Solid Ice	NaCl & MgSO$_4$	1 M	Vu et al. 2016
	NaCl & MgSO$_4$	3.07/1.44 M	Vu et al. 2016
	H$_2$O over MgSO$_4$	Pure	Carlson et al. 2009

	H$_2$O over MgSO$_4$•7H$_2$O	Pure	Carlson et al. 2009
Liquid	NaCl & MgSO$_4$	1 M	Vu et al. 2016
	NaCl & MgSO$_4$	3.07/1.44 M	Vu et al. 2016

3.3 Results and Discussion

3.3.1 The Particulate Ice Surface

The composition of a planetary surface is indicative of its evolution and chemical history, so understanding the surface is necessary to understand the body's system as a whole. To simulate the surface of ocean worlds (e.g. Moore et al., 2009; Nelson et al., 2018; Molaro et al., 2019), we created particulate ice with the following liquid solutions of interest: 32% methanol (Hodyss et al., 2009), 3% hydrogen peroxide (Carlson et al., 1999; Carlson et al., 2009), 1 M sulfuric acid (Carlson et al., 2002; Dalton II et al., 2013), equimolar 1 M NaCl and MgSO$_4$ (Vu et al., 2016), saturated 3.07/1.44 M NaCl and MgSO$_4$ (Vu et al., 2016), and 2.46 M beta-alanine and glycine, separately (Pappalardo et al., 2013). In addition to these particulate ice samples, we experimented with measuring gypsum, a hydrated sulfate, through a layer of particulate H$_2$O-ice to demonstrate the ability of Raman spectroscopy to measure targets through the first few millimeters of surface depth.

3.3.1.1 Solutions based on Radiation Products: Methanol, Hydrogen Peroxide, and Sulfuric Acid

Finding organics and/or the byproducts of radiation coming into contact with organics, such as sulfuric acid, would be one step towards determining habitability on or below the surface of ocean worlds. Using a compact portable Raman spectrometer in our laboratory setting at 5 meters, we successfully measured a 32% CH$_3$OH (methanol) solution in distilled H$_2$O (Figure 3.5a), a 3% H$_2$O$_2$ (hydrogen peroxide) solution in distilled H$_2$O (Figure 3.5b) and 1 M H$_2$SO$_4$ (sulfuric acid) in distilled H$_2$O (Figure 3.5c).

Detecting methanol at the surface of ocean worlds, either as a photochemical product of methane and water or as a deposition product from plumes (e.g. Enceladus; Hodyss et al., 2009), would be important in determining habitability. The detection of methanol could either be due to plume deposition from the subsurface ocean or photochemical processes at the surface, and both topics are of interest for missions to the ocean worlds. We measured a solution of 32% methanol (CH_3OH) in distilled H_2O at 5 meters using our system (Figure 3.5a). In particular, we can easily resolve the C-O stretch, the CH_3 bend, and the CH symmetric and anti-symmetric stretch from the methanol molecule (Mammone et al., 1980) (Table 3.2). In addition, the symmetric stretch of H_2O-ice and the broad band liquid-H_2O peak are present in the ~3000-3500 cm^{-1} region, indicating that the methanol is in a solution with water.

The presence of hydrogen peroxide on the surface of Europa has been indicated by the 3.50-µm feature in spectra from Galileo's near-infrared mapping spectrometer (NIMS) (Carlson et al., 1999). We measured a solution of 3% hydrogen peroxide (H_2O_2) in distilled H_2O at 5 meters using our system (Figure 3.5b). A successful measurement of the solution includes the presence of the O-O stretch feature at 882 cm^{-1}, indicative of the hydrogen peroxide molecule (Sharma et al., 2019). The broad band water and water ice features seen between 3000 cm^{-1} and 3500 cm^{-1} indicate the presence of H_2O-liquid and H_2O-ice.

Hydrated sulfuric acid is thought to be a product of radiolysis on the surface of Europa due to energetic particle bombardment (Carlson et al. 2002). We measured a solution of 1 M H_2SO_4 in distilled H_2O at 5 meters using our system (Figure 3.5c). Since sulfuric acid is dangerous to handle, especially when in a particulate form, we used a milliliter dropper to create ice nodules in the liquid nitrogen. As a result, the grain size of this ice sample is much larger than the other particulate ice surface samples. We were able to successfully measure this sample as indicated by the presence

of the symmetric stretch feature of the SO_4^{2-} ion and the symmetric bend feature of SO_4 (Tomikawa et al., 1998) (Table 3.2). It is noted in Tomikawa et al. (1998) that SO_4^{2-} symmetric stretch feature increases in intensity with decreasing concentration of H_2SO_4 and decreasing temperature. The smaller resolution feature at 455 cm^{-1} is due to the symmetric bend of the HSO_4^- and/or SO_4^{2-} ions. They also state that the Raman bands arising from HSO_4^- ions decrease rapidly in intensity with decreasing concentration. Because of this, we do not see the feature at ~1040 cm^{-1} due to the symmetric stretch of the HSO_4^- ions, as would be seen in higher concentrations of warmer samples. As previously noted, the symmetric and antisymmetric stretch features of H_2O ice are notable in the 3000 cm^{-1} to 3500 cm^{-1} region.
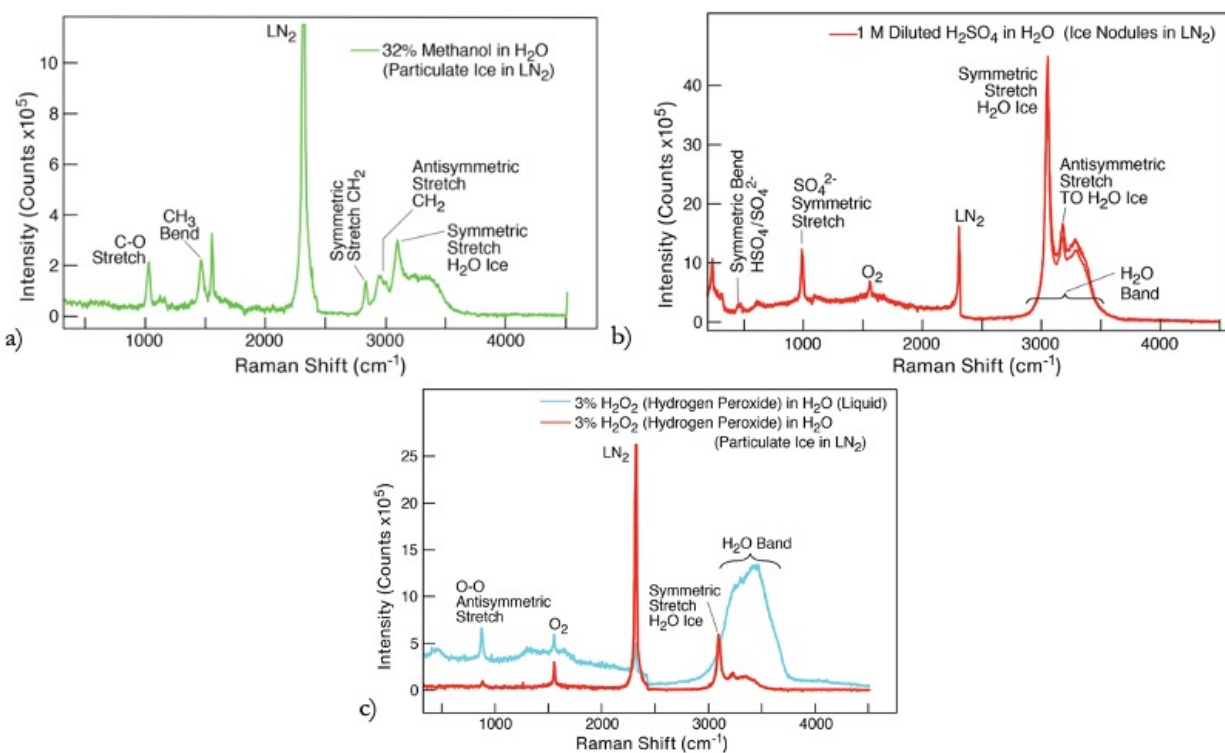
Figure 3.5: Remote Raman spectra of a) particulate ice solution of 32% methanol (CH₃OH) in distilled H₂O, b) particulate ice solution of 3% hydrogen peroxide (H₂O₂) in distilled H₂O, and c) ice nodules of 1 M sulfuric acid (H₂SO₄) in distilled H₂O measured at a distance of 5 m in a lighted laboratory setting.

3.3.1.2 Particulate Frozen Brines: Equimolar and Saturated

Data from NIMS on Galileo suggest that Jupiter's icy moons have hydrated sulfates distributed on their surface (McCord et al., 2011). Identifying these salt solutions will aid in our understanding of the chemical properties and past processes at the surface of these bodies. Raman studies of hydrated minerals of a wide variety have been published previously (Wang et al. 2006). Although NaCl is *not* Raman active, some studies have indicated the ability to measure the presence of NaCl within other solutions based on the phase of the salt (Durickovic et al., 2010). Using a compact portable Raman spectrometer in our laboratory setting at 5 meters, we successfully measured a 1 M NaCl and 1 M $MgSO_4$ solution in distilled H_2O (Figure 3.6a) and a 3.07 M NaCl and 1.44 M $MgSO_4$ solution in distilled H_2O (Figure 3.6b). These solutions were created and studied by Vu et al. (2016) as simulants of the liquid interior of ocean worlds.

As mentioned, NaCl is *not* Raman active but the presence of $MgSO_4$ is seen clearly in our spectra (Figure 3.6a,b). We show the particulate ice and liquid spectra in each subfigure to show the difference in the resolution of the symmetric and antisymmetric stretch in H_2O-ice versus liquid H_2O. The most intense peak is the symmetric stretch of SO_4, seen at 983 cm^{-1} and the symmetric bend of SO_4 is seen at 449 cm^{-1} (Wang et al., 2006), shown in Table 3.2. As introduced previously, the Raman features for liquid H_2O and H_2O-ice can be seen in the 3000 cm^{-1} to 3500 cm^{-1} region.
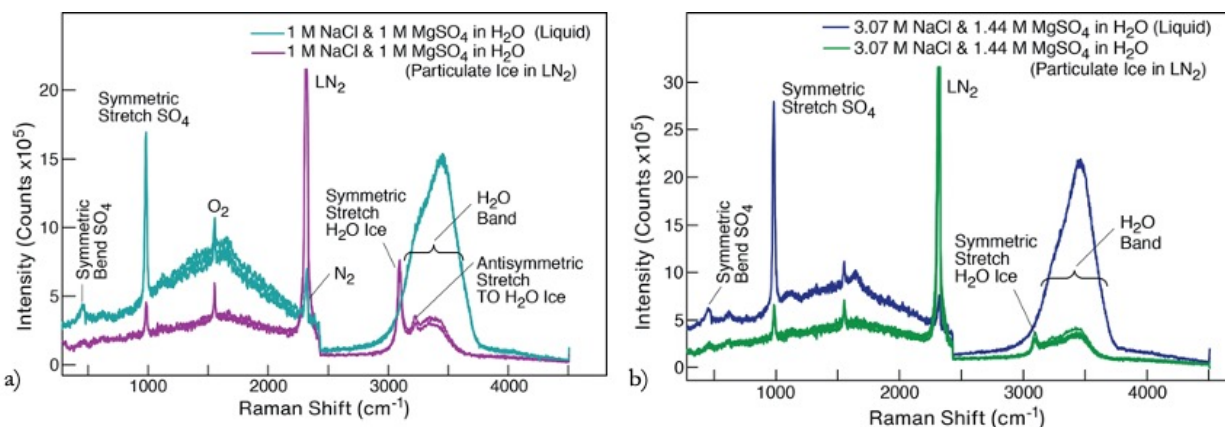
Figure 3.6: Remote Raman spectra of a) particulate ice solution of 1 M NaCl and 1 M MgSO₄ in distilled H₂O and b) particulate ice solution of 3.07 M NaCl and 1.44 M MgSO₄ in distilled H₂O measured at a distance of 5 m in a lighted laboratory setting.

3.3.1.3 Amino Acids: Glycine and Beta-alanine

Amino acids are the building blocks of proteins, which is an essential part of life as we understand it. The ability to detect amino acids on planetary bodies is necessary in the search for life outside of Earth and has been outlined in NASA's Astrobiology Strategy (2015). Using a compact portable Raman spectrometer in our laboratory setting at 5 meters, we successfully measured particulate ice samples from a 2.46 M glycine solution in distilled H_2O (Figure 3.7a) and a 2.46 M beta-alanine solution in distilled H_2O (Figure 3.7b), using our system. We also show the spectrum of liquid solution for comparison and to highlight some of the subtle peaks in the particulate ice spectrum. The strongest characteristic Raman peaks for the amino acids glycine and beta-alanine (Figure 3.7), are shown in Table 3.2, as assigned in Culka et al. (2010) and Acosta-Maeda et al. (2018).

Table 3.2. The peak positions of major features in the samples measured, shown in Figures 3.5 - 3.11. The associated literature references for the assignments are also included.

Sample	Literature Reference	Wavenumber (cm⁻¹)	Assigned Molecular Vibration

Methanol	Lemos and Camargo et al. (1990)	1024	C-O Stretch
		1466	CH_3 Bend
		2836	CH_3 Symmetric Stretch
		2947	CH_3 Anti-symmetric Stretch
H_2O_2	Sharma et al. (2019)	882	O-O Stretch
H_2SO_4	Tomikawa et al. (1998)	455	HSO_4^-/SO_4^{2-} Symmetric Bend
		986	SO_4^{2-} Symmetric Stretch
Equimolar NaCl & $MgSO_4$	Wang et al., 2006	449	SO_4 Symmetric Bend
		983	SO_4 Symmetric Stretch
Saturated NaCl & $MgSO_4$	Wang et al., 2006	449	SO_4 Symmetric Bend
		983	SO_4 Symmetric Stretch
Glycine	Culka et al. (2010)	895	C-CN Symmetric Sretch
		1325	CH_2 Wagging
Beta-Alanine	Acosta-Maeda et al. (2018)	876	C-CN Symmetric Stretch
		935	CH_2 Rocking
		1051	C-N Symmetric Stretch
		1416	COO- Symmetric Stretch
H_2O Ice	Whalley (1977)	1552	O_2
		2322	LN_2
		3096	H_2O ice Symmetric Stretch
		3234	H_2O ice Anti-Symmetric Stretch TO
H_2O Ice on Gypsum		418 & 489	SO_4 Symmetric Bend Doublet
		1010	SO_4 Symmetric Stretch
		1138	SO_4 Anti-Symmetric Stretch
		3096	H_2O ice Symmetric Stretch
		3428	H_2O in Gypsum Symmetric Stretch
		3504	H_2O in Gypsum Anti-symmetric Stretch
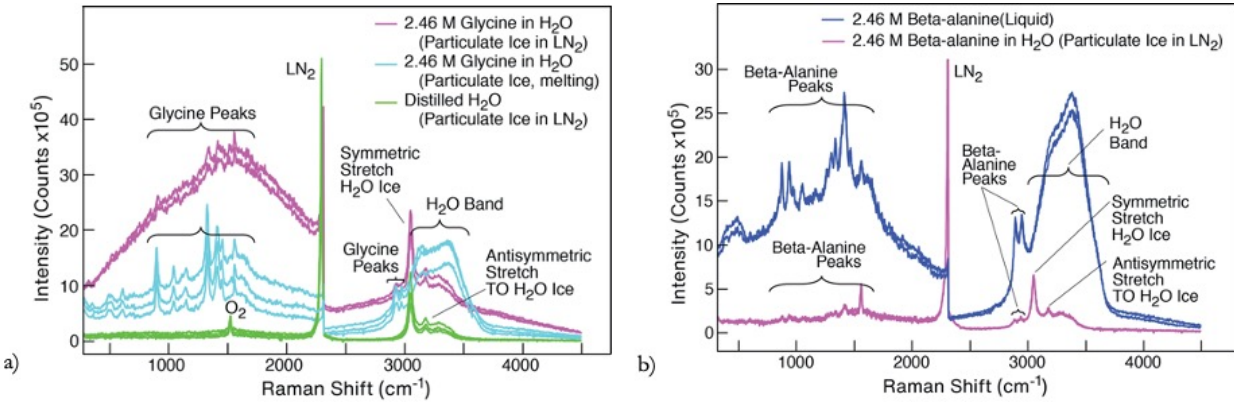
Figure 3.7: Remote Raman spectra of a) particulate ice solution of 2.46 M glycine in distilled H2O and b) particulate ice solution of 2.46 M beta-alanine in distilled H2O measured at a distance of 5 m in a lighted laboratory setting.

3.3.1.4 Combined hydrated minerals, salts and H_2O-ice

In order to replicate a mission style encounter with solutions, we showed that Raman spectroscopy can penetrate a top layer of particulate ice to measure a mineral or salt of importance below. This is an advantage of Raman spectroscopy in the exploration of ocean worlds as opposed to other remote spectroscopic techniques such as reflectance spectroscopy, which can only penetrate the top microns of a surface. Penetrating the top layer of ice will be important for learning about the chemical processes that occur on the surface of ocean worlds and in gaining insight into habitability.

Understanding the spectrum of pure H_2O is helpful in distinguishing the solute features from the solvent features in the solutions measured in this study. Being able to detect H_2O is essential for an instrument participating in the search for past and present life and has been outlined as a detection strategy to finding signs of life in the NASA Astrobiology Strategy (2015). Figure 3.8a shows the spectrum of distilled particulate H_2O-ice. The broad water feature is present and the sharper peaks due to the phase of the H_2O-ice is noticed in the symmetric stretch feature and the antisymmetric stretch TO feature (Whalley 1977).

37

Gypsum ($CaSO_4 \cdot 2H_2O$) is a hydrated mineral that we used to demonstrate the ability of our system to detect the presence of a target through a layer of pure particulate H_2O-ice (Figure 3.8b). As seen in the salt solutions, the SO_4 symmetric and antisymmetric stretch features are present at 1010 and 1138 cm^{-1}, respectively, and the symmetric bend doublet of SO_4 is present at 418 and 489 cm^{-1}. In the high frequency region near the H_2O-ice stretch regions discussed above, the symmetric and antisymmetric stretch of the H_2O molecule in the gypsum mineral is present at 3428 and 3504 cm^{-1}, respectively. This feature is noticeably separate from the H_2O features from the particulate ice in Figure 3.8a.

Carlson et al. (2009) outlined the possibility of crystallized salt hydrates as a result of flash evaporation, simulated in Figure 3.4c and measured in Figure 3.8c. This sample was created from a mixture of the melted particulate ice salt brines evaporating over a long weekend and leaving behind crystals we assumed to be $MgSO_4$ or $MgSO_4 \cdot 7H_2O$. From the spectrum in Figure 3.8c, we can identify the SO_4 symmetric stretch feature as well as a faint feature noted as the symmetric bending mode of SO_4. The crystallized brine materials were very small and scattered all over the petri dish as shown in Figure 3.4c, so only a few crystals fell in the area of laser beam resulting in a weaker Raman signal. There is a weak contribution in the broad band water region which may denote that some of the crystals are hydrated.
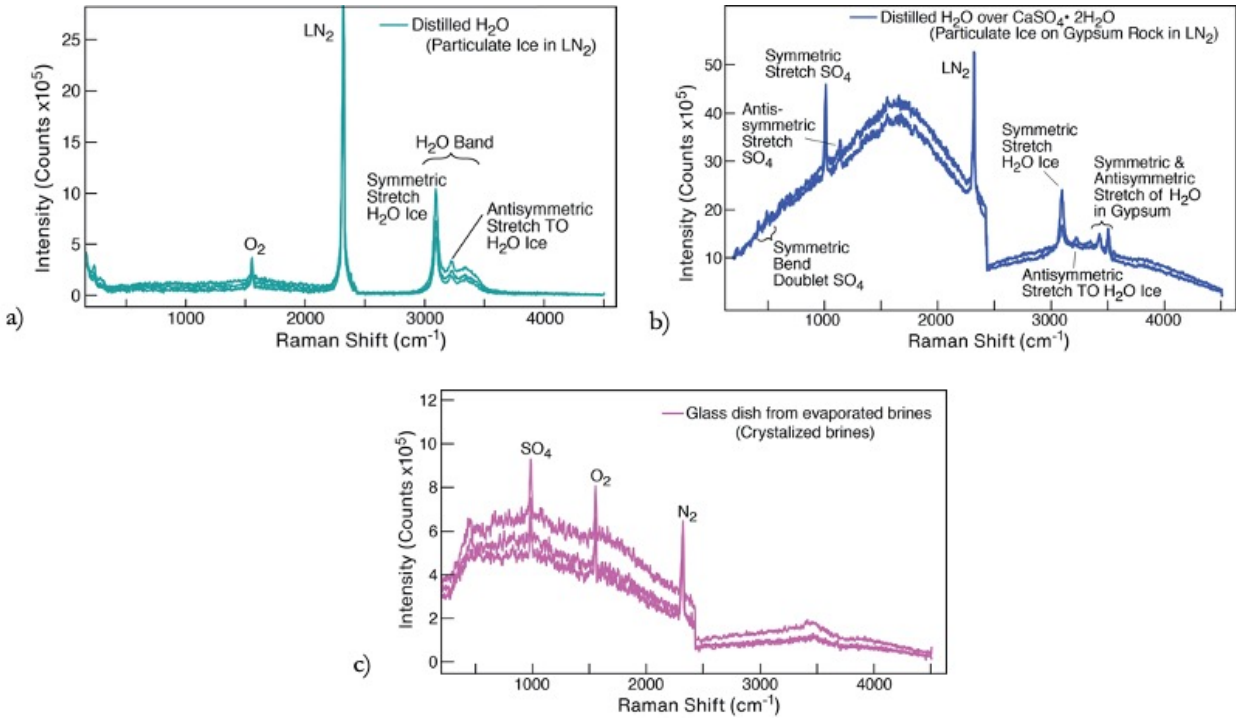
Figure 3.8: Remote Raman spectra of a) distilled H₂O particulate ice over a gypsum rock, b) distilled H₂O, and c) crystalized brine solutions in a glass dish measured at a distance of 5 m in a lighted laboratory setting.

3.3.2 The Solid Ice Shell

All ocean worlds thought to possess present-day interior global oceans have an outer icy shell that protects these expansive, volatile reservoirs from the low-temperature, low-pressure environments of space (Hendrix and Hurford et al., 2018). The icy shell of these bodies could contain both inclusions of the ocean below and remnants of the overturned and possibly tectonically active surface above (Postberg et al. 2009; Howell and Pappalardo, 2018; Howell and Pappalardo, 2019). We simulated this icy layer by freezing liquid solutions to form solid ice. In our ice shell simulation, we used salt brine solutions, namely the equimolar 1 M NaCl and MgSO₄ and saturated 3.07/1.44 M NaCl and MgSO₄ (Vu et al., 2016), and pure H₂O. We experimented further with the ability of Raman spectrometers to penetrate and measure samples by leaving salts below the solid H₂O-ice layer (Figure 3.10). This ability will not only be useful at the surface as

previously discussed, but also in the solid ice shell onboard any deep subsurface or ocean access exploration platforms (Hendrix and Hurford et al., 2018).

3.3.2.1 Frozen Brines: Equimolar and Saturated

Because the oceans on icy moons are thought to be brines (Vance et al. 2016), we measured the solid ice phases of the salt solutions introduced above. Figure 3.9a shows the spectrum for the solid ice equimolar solution. Due to the increased penetration depth of the measurement in solid ice as opposed to particulate ice, the Raman features denoting the presence of the sulfate ion and H_2O molecule appear more intense. We are able to distinguish the TO and LO antisymmetric stretch features in H_2O-ice (Whalley, 1977) as well as the antisymmetric stretch of the sulfate ion.

In the solid ice spectrum of the saturated solution (Figure 3.9b), we see similar peaks. The peaks are more intense in this spectrum since the concentration of the sulfate ion is higher, namely 1 M in the equimolar solution and 1.44 M in the saturated solution.
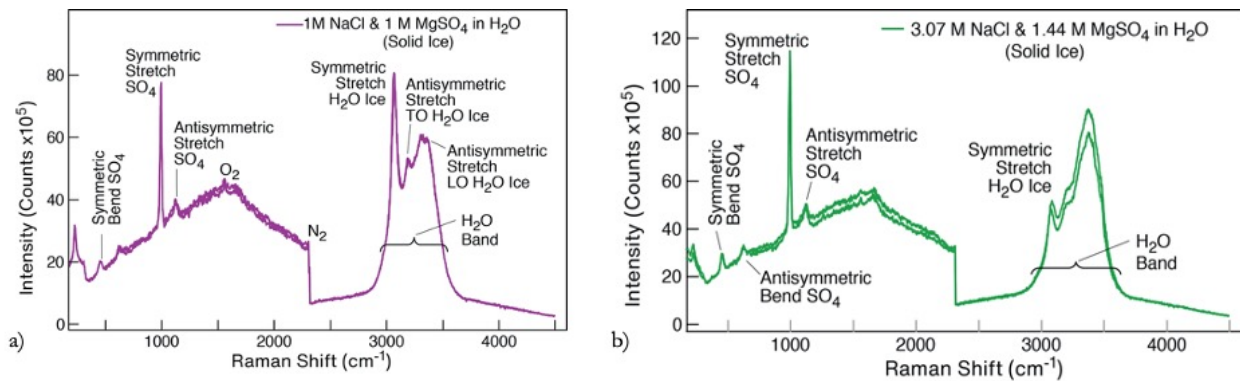
Figure 3.9: Remote Raman spectra of a) solid ice solution of 1 M NaCl and 1 M MgSO$_4$ in distilled H$_2$O and b) solid ice solution of 3.07 M NaCl and 1.44 M MgSO$_4$ in distilled H$_2$O measured at a distance of 5 m in a lighted laboratory setting.

3.3.2.2 Pure salts through solid ice

For the sake of applicability of our data to events that may take place during a mission to an ocean world, we measured several ocean world-relevant salts covered by a block of solid H_2O-ice. Figure 10a shows the spectrum of a sample we created by first filling a glass beaker with liquid nitrogen followed by a few centimeters of anhydrous magnesium sulfate and lastly, liquid H_2O, which quickly solidified to form a solid H_2O-ice layer above the anhydrous magnesium sulfate. The ice was measured to be a few centimeters thick, though an exact measurement was not feasible. All the peaks for anhydrous magnesium sulfate previously discussed are present (symmetric and antisymmetric stretch, symmetric and antisymmetric bend), showing that the incident light successfully penetrated the ice to reach and produce Raman photons from the magnesium sulfate underneath. The water band present in this spectrum is indicative of the H_2O-ice layer given that the symmetric stretch peak is sharp.

Next, we measured hydrated magnesium sulfate through a solid H_2O-ice layer (Figure 3.10b) using the same process. The main difference is seen in the intensity of the H_2O bands, indicating the presence of H_2O within the salt crystal lattice, i.e. a hydrated mineral. Another important feature of this spectrum is the change of the water band over each of the three measurements taken. The intensity of the water band, and especially the intensity of the symmetric stretch feature of H_2O, shrinks over time indicating that there is less H_2O-ice present as time goes on, i.e. the ice was melting.
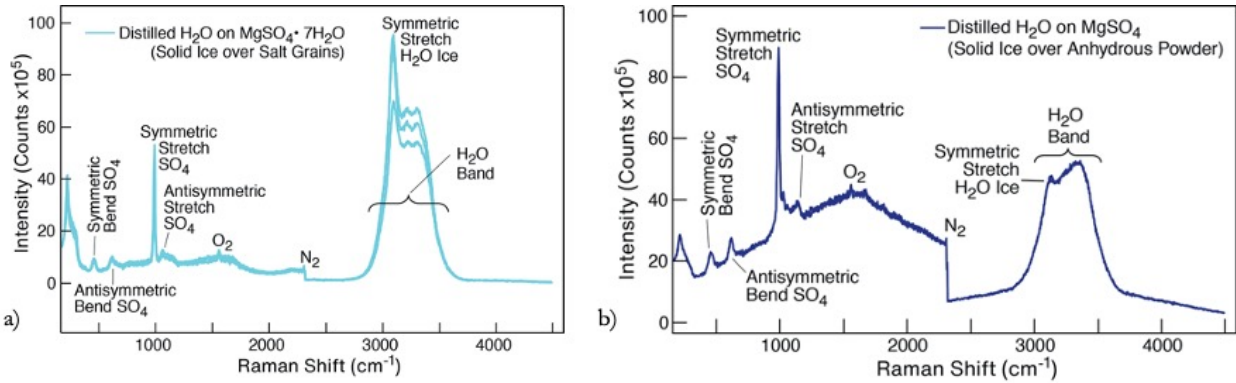
Figure 3.10: Remote Raman spectra of a) solid ice distilled H₂O over MgSO₄·7H₂O salt grains and b) solid ice distilled H₂O over MgSO₄ measured at a distance of 5 m in a lighted laboratory setting.

3.3.3 The Liquid Ocean

The liquid ocean is the final "layer" of ocean worlds that we simulated in this experiment (Figure 3.1). The salt brine solutions used in simulating the previous two layers were measured in their liquid forms to provide an ocean simulant. We chose these brines to simulate the ocean for a number of reasons including evidence from Zolotov et al. (2007), Postberg et al. (2009), and Vu et al. (2016). Relating to Enceladus, Cassini revealed the presence and detection of water rich plumes near the south pole (Waite et al., 2006). The models described in Zolotov et al. (2007) determined that if there still exists an aqueous phase on Enceladus, it would be composed of a salt-ice-brine, with the possibility of organics as well. Postberg et al. (2009) concluded that many of the ice grains from Enceladus' plumes dominate Saturn's E-ring and are composed, in part, of siliceous components that could be evidence of the interaction between a liquid water ocean and the rocky core of Enceladus. Similarly, Europa's surface texture suggests that the liquid from the subsurface ocean can occasionally be found frozen at the surface and can thus reveal information about the composition of the oceanic interior (Vu et al., 2016). Each of these studies indicates the applicability of the salt brines measured in this experiment to the subsurface ocean of ocean worlds.

42

3.3.3.1 Liquid Brines: Equimolar and Saturated

On both Enceladus and Europa, the surface composition has been previously studied to decipher the likely composition of the subsurface oceans (Zolotov et al., 2007; Vu et al., 2016). We used the equimolar and saturated salt solutions from Vu et al. (2016) to simulate ocean world liquids. Figure 3.11a shows the successful measurement of the equimolar solution in liquid form, indicated through the broad H_2O band in the 3000 cm^{-1} to 3500 cm^{-1} region. The spectrum in Figure 3.11b warrants a parallel discussion, since the solutions measured contain the same components, but show a stronger sulfate ion feature due to the increase in concentration of $MgSO_4$. The peak positions of theses features can be found in Table 3.2.
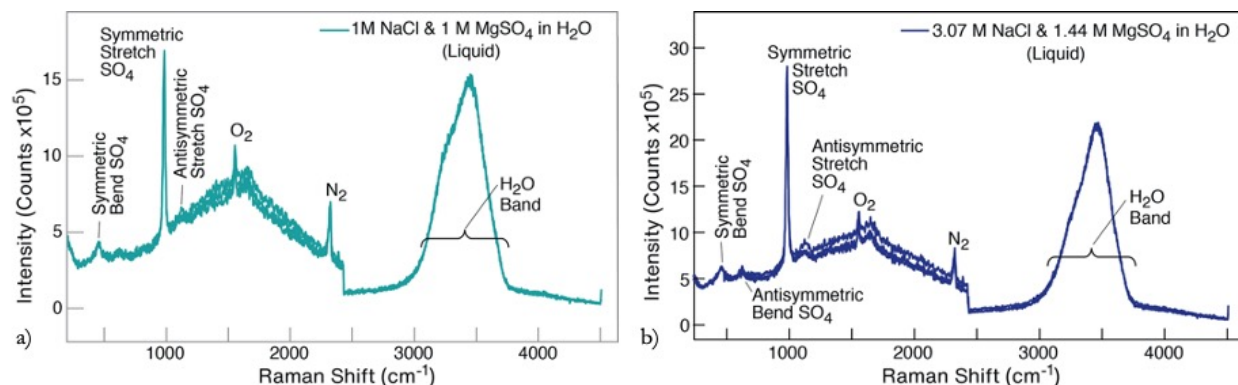
Figure 3.11: Remote Raman spectra of a) liquid solution of 1 M NaCl and 1 M MgSO4 in distilled H2O and b) liquid solution of 3.07 M NaCL and 1.44 M MgSO4 in distilled H2O measured at a distance of 5 m in a lighted laboratory setting.

3.4 Conclusion

We successfully measured ocean-world-relevant icy and liquid samples using a compact portable remote Raman spectrometer at 5 meter range. The samples included simulants of the particulate icy surface, with a composition controlled by radiation, impacts, and possible plume deposits, simulants of the icy shell, indicative of surface chemistry and interior ocean chemistry,

and simulants of the saline liquid ocean (Figure 2.1). The Raman spectra presented have high signal to noise ratio and highlight the unique capabilities for the technique in exploring ocean worlds through the surface and icy shell to the interior ocean. Proposed and potential future missions such as the Europa Lander and subsurface ocean access platforms should evaluate the inclusion of a remote Raman spectrometer as a science-enabling technology for habitability and life-detection missions, and a detection-enhancing technique for investigations of ice and ocean chemistry.

Chapter 4: Revolutionizing the Data Return Yield for Imaging Spectroscopy of the Lunar Surface Using Onboard Prioritization Algorithms

Abstract New methods for onboard analysis of hyperspectral data are needed as planetary missions collect ever-larger data volumes, preceding the technological advancements for larger downlink bandwidth. Onboard processing algorithms that screen data in real time for absorption features of interest is one solution to this problem. Various minerals, volatiles, and organics that are significant to planetary exploration are noted in previous studies by characterizing the presence of absorption features in hyperspectral pixels. UCIS-Moon is an imaging spectrometer in development for a lunar lander with specific applications for detecting and understanding the role of volatiles and unique minerals on the lunar surface. One of the particular capabilities of this instrument, which will aid in characterizing volatiles on the moon, is its spectral range from 0.6 to 3.6 μm. This spectral range is defined to include prominent spectral features from OH, H_2O, and organics. The prioritization algorithms used in this study to characterize the presence of such volatiles and other minerals of interest on the lunar surface include a Continuum Interpolated Band Ratio (CIBR) method given known bands of interest and the Reed-Xiaoli (RX) anomaly detection method incorporated to catch spectra of interest with spectral features not indicated by previous studies. To date, there has not been an instrument with a primary mission to collect spectral data of the lunar surface out to 3.6 μm. In order to test these potential onboard algorithms for their efficiency in optimizing data uplink for UCIS-Moon, we developed a dataset that is representative of the innovative spectral range that UCIS-Moon will measure. We extrapolated thermally corrected Moon Mineralogy Mapper (M^3) data using known reflectance in the necessary range from existing RELAB spectra and added a thermal component to the extrapolated spectrum to

simulate the lunar environment out to 3.75 μm. The extrapolated dataset was thermally corrected before being used to test the proficiency and compute time of the aforementioned optimization algorithms that will prioritize uplink of spectra with absorption features of interest, indicating the presence of volatiles and particular minerals.

4.1 Introduction

The data collected by imaging spectrometers with increasing optical efficiency has outgrown the available bandwidth to transmit data back to Earth, resulting in a massive loss of information. Data prioritization is one way to optimize data storage by choosing to only transmit data that is relevant to the science objectives of the mission, instead of degrading an entire data set. The Moon Mineralogy Mapper (M^3) onboard Chandryaan-1 (Green et al., 2011) was intended to collect data during four optical periods over the course of the two-year nominal mission for the spacecraft. Instead, it encountered two issues that reduced its ability to collect the data and was operational during two optical periods rather than four. A thermal issue and the loss of a star tracker led the mission team to re-plan the extent and collection of measurements of the lunar surface. One of the changes made to the observational requirements was a reduction in the spatial coverage of measurements collected in Target Mode, where the spatial and spectral resolution were heightened. This resulted in an M^3 data set with much lower spectral resolution than desired (Boardman et al., 2011). One option that was not available to the instrument at the time was data prioritization. A simple data prioritization algorithm built-in to future imaging spectrometers has the potential to provide a low bandwidth mission, such as a commercial mission, with prioritized scientifically

interesting data or act as a backup processer in case of any instrument mishaps, such as the issues M^3 encountered.

Future imaging spectrometers with objectives to better characterize the Moon are of great interest to the scientific community (Pieters et al., 2018). Some of the absorption features of particular interest hinted at in M^3 data cannot be fully characterized until we study the Moon with extended wavelength ranges. For the study of water ice (Pieters et al., 2011; Cheek et al., 2011; Zurber et al., 2012; Li and Miliken, 2017; Li et al., 2018) and organics (Matthewman et al., 2015), a spectral range extended to 3.6 μm is necessary to distinguish various hydrated states. Many of the upcoming imaging spectroscopy missions to the Moon include this extended spectral range and aim to collect measurements that will distinguish hydration on the lunar surface, i.e. OH, H_2O, H_2O ice. UCIS-Moon is a compact imaging spectrometer that will travel to the surface of the Moon onboard a commercial lander. This instrument will collect image cubes from 0.6 to 3.6 μm with high spatial and spectral resolution and will benefit from onboard data optimization. UCIS-Moon plans to achieve this by screening the collected spectra onboard for absorption features indicative of volatiles and minerals of interest, prioritizing the uplink of the datasets collected. UCIS-Moon is being created from its heritage developments (Van Gorp et al., 2014), but onboard data prioritization is a key feature that requires testing and verification before full inclusion on the final instrument.

Simple, non-complex onboard prioritization algorithms will allow the technique more flexibility in breadth of use since a simple algorithm will not be heavily constrained by onboard processing time and power requirements. We tested the use of two onboard prioritization algorithms that are efficient and non-complex for potential use onboard future imaging

spectrometers aimed at characterizing the lunar surface, namely continuum interpolated band ratio (CIBR) and Reed-Xiaoli (RX) anomaly detection (Reed and Xiaoli, 1990). The CIBR method aims to screen spectra for particular absorption features indicative of minerals and volatiles of interest, outlined in Table 4.1. In addition to these minerals and volatiles, UCIS-Moon is also interested in the presence of unknown minerals and volatiles. Since the CIBR method is built to find previously identified features of interest, we include the RX anomaly detection method to function as a safety net for spectra of interest to the scientific community not highlighted in previous literature or Table 4.1. The details of these methods are discussed in section 4.2.1.

Table 4.1. The minerals and volatiles of interest to UCIS-Moon with the location of their respective absorption features in microns. These locations are used in the prioritization algorithms.

Minerals and Volatiles of Interest	Feature Location ▼
Hematite	0.86 μm
Olivine	1 μm
Pyroxene	1 and 2 μm
Mg-spinel	2 and 2.9 μm
OH	2.8 μm
H_2O	2.9 μm
H_2O Ice	3.1 μm
Organics	3.4 μm

In order to determine the feasibility of these algorithms onboard, we must test them on a simulant dataset to ensure their proficiency. M^3 is the largest spectroscopic data set characterizing the lunar surface, covering over 90% of the surface (Boardman et al. 2011) (Figure 4.1). As previously introduced, UCIS-Moon has a spectral range from 0.6 to 3.6 μm, but M^3 data only extends to 3.0 μm. In order to test the onboard prioritization algorithms, we created a dataset simulant of the lunar surface ranging from 0.55 to 3.75 μm by extrapolating M^3 spectra using

Reflectance Experiment Laboratory (RELAB) data. The method used to create the simulant dataset is described in more detail in section 4.2.2, but the finalized dataset is composed of thousands of M^3 pixels (Table 4.2) extrapolated using RELAB spectra (Table 4.3) to 3.75 µm, with an added thermal component calculated using the empirical method described in Li and Milliken (2016) to simulate the lunar environment as detected by an orbiting imaging spectrometer.

In all, this study aims to characterize the use of onboard prioritization for the use onboard future imaging spectrometers with missions to the Moon. We perform this characterization by testing the algorithms proficiency on a dataset simulant of the lunar surface from 0.6 to 3.6 µm. Since this dataset has not been collected yet, we extrapolated previously existing thermally corrected spectra of the lunar surface using laboratory measurements of Apollo and lunar simulant soils that extend into the range of interest. We then added absorption features of interest and a lunar thermal component to the existing and extrapolated portions of the spectra before testing the outlined prioritization algorithms for proficiency. Section 4.2 outlines the methods used for onboard prioritization and in extrapolating spectra in more detail and section 4.3 discusses the results and implications of the study.
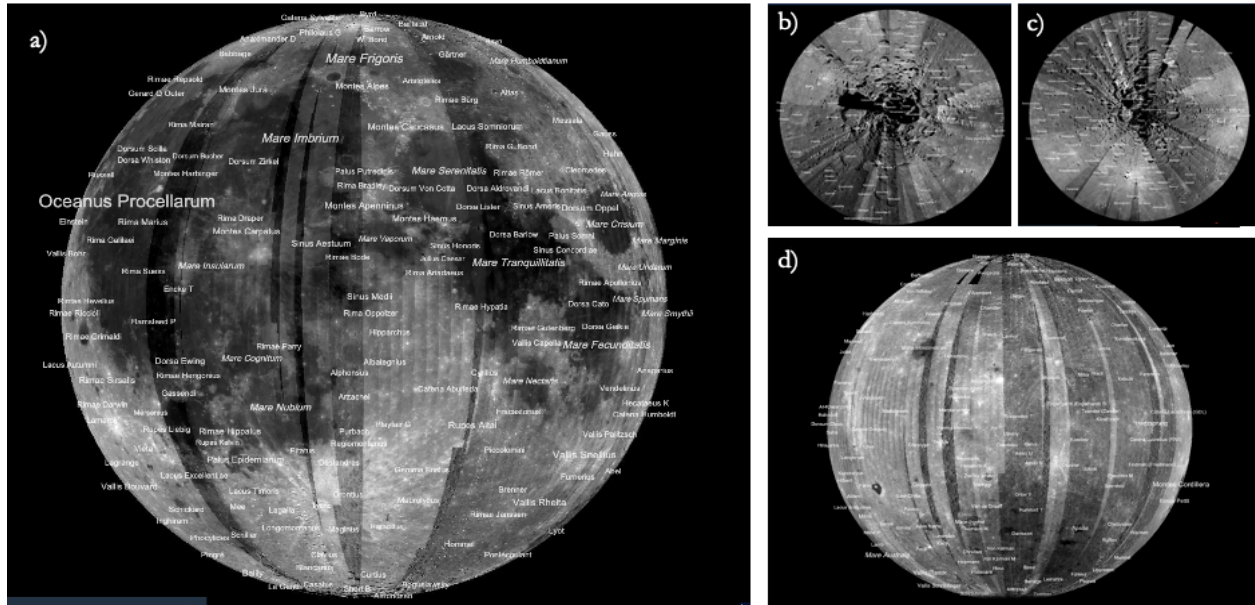
Figure 4.1: A map of M³ coverage of the a) lunar near-side, b) lunar north pole, c) lunar south pole, and d) the lunar far-side. These images were produced using Arizona State University's QuickMap system.

4.2 Methods

4.2.1 Prioritization Algorithms

We take advantage of previous methods for novelty detection in order to prioritize our spectral data set for signatures indicative of the particular mineral and volatile interests of UCIS-Moon (Table 4.1). The two methods tested in this study for prioritizing lunar imaging spectra are continuum interpolated band ratio (CIBR) detection, (e.g. Conel et al. (1989), Bruegge et al. (1990), Manolakis et al. (2016), Thompson et al. (2015)), and Reed-Xiaoli (RX) anomaly detection (e.g. Reed and Xiaoli (1990), Guo et al. (2016), Zhao et al. (2016) and Wang et al. (2018)). These methods are both simple and feasible for use onboard.

4.2.1.1 Continuum Interpolated Band Ratio

Continuum Interpolated Band Ratio (CIBR) is a simple technique used to determine the presence of particular materials in hyperspectral data. This technique fundamentally uses the ratio between the reflectance value at a given band and the continuum values nearby that band to determine the presence of a feature. When the following ratio is less than one, there is an absorption feature present,

$$CIBR = \frac{L(\lambda_{center})}{\omega_{left}*L(\lambda_{left}) + \omega_{right}*L(\lambda_{right})}$$ Eq. 4.1

where L is the radiance at a given band, i.e. $\lambda_{center}, \lambda_{left}, \lambda_{right}$, and $\omega_{left}, \omega_{right}$ are the weighting coefficients that sum to unity. As described in Manolakis et al. (2016), we use,

$$\omega_{left} = \frac{\lambda_{right}-\lambda_{center}}{\lambda_{right}-\lambda_{left}} \text{ and } \omega_{right} = \frac{\lambda_{center}-\lambda_{left}}{\lambda_{right}-\lambda_{left}}.$$ Eq. 4.2

It is important to note that noise will contribute to this ratio and a perfect value of 1 is rarely seen. Instead of using the radiance at nearby bands, we used the continuum radiance given by a calculated convex hull. Using the convex hull for $L(\lambda_{left})$ and $L(\lambda_{right})$ produces a more dramatic difference between nearby bands and the band of interest, increasing the classification accuracy of the CIBR method. Using the convex hull, cont, in Eq. 4.1, it then becomes,

$$CIBR = \frac{L(\lambda_{center})}{\omega_{left}*cont(\lambda_{left}) + \omega_{right}*cont(\lambda_{right})}.$$ Eq. 4.3

To be conservative in our prioritization of spectra with the aforementioned features, we use a threshold of CIBR = 0.93 to determine the presence of a feature. This value was determined by

considering the false positive and true positive rates (Figure 4.2). The receiver operating characteristic (ROC) curve shows that the most spectra are correctly classified *and* the least spectra are misclassified when the threshold value is 0.93. Anything below 0.93 CIBR is indicated to have the absorption feature present. For applications to UCIS-Moon, it is fundamentally important that we prioritize spectra with an absorption feature, no matter which one it may be. A more complex algorithm may include the determination of the absorption feature for use in a mineral map.
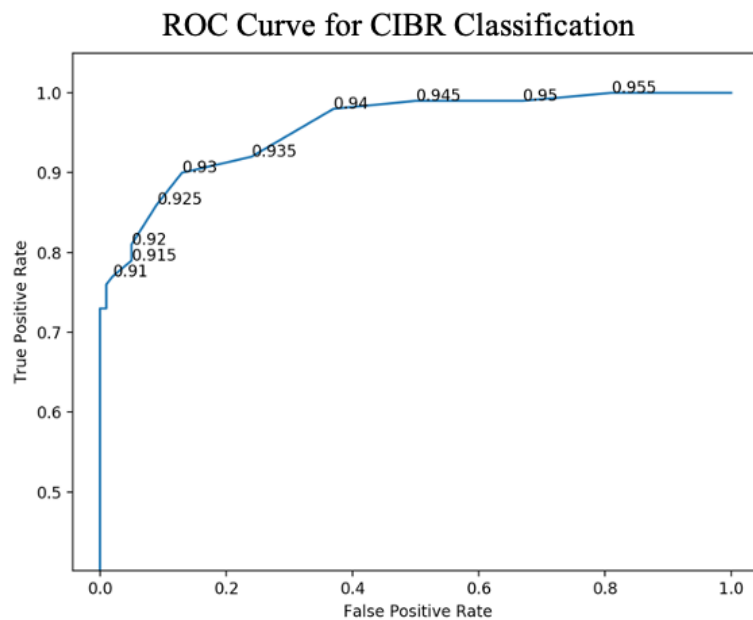
Figure 4.2: A receiver operating characteristic (ROC) curve used to define the classification accuracy of binary classifiers, such as CIBR. This curve shows that 0.93 is the ideal threshold to classify the presence of an absorption feature.

4.2.1.2 Reed-Xiaoli Anomaly Detection

Anomaly or novelty detection techniques aim to identify spectra with absorption features that could be of interest but are not previously defined. When exploring the lunar surface for volatiles, it will be important to include a detection method of this kind in case we find something

unexpected. The RX anomaly detection method is often used for hyperspectral data cubes since an anomaly can be identified by comparing each pixel to its neighbors. Using the mean and covariance of the spectra in neighboring pixels, we calculate the matrix δ_{Rx} (Eq. 4.4), describing the relationship of each target band to the distribution of the neighboring pixels' bands;

$$\delta_{Rx}(R_{ij}) = \left(R_{ij} - \mu_B\right)^T {\textstyle\sum_B}^{-1}(R_{ij} - \mu_B), \qquad\qquad \text{Eq. 4.4}$$

where R_{ij} is the reflectance values in the target spectrum, μ_B is the mean of the neighboring pixels, and $\sum_B$ is the covariance of the neighboring pixels. The resulting matrix has the same size as the covariance matrix, # of bands x # of bands (650 x 650).

In order to test the proficiency of these prioritization algorithms, we created a lunar simulant dataset from 0.5 to 3.75 μm at a 5 nm spectral resolution. The creation of this dataset is described in section 2.2 and the results of the study are presented in section 3.

4.2.2 Creating a Simulant Dataset

The first step in understanding the proficiency of the proposed onboard algorithms is to create a simulant dataset for the UCIS-Moon mission. The challenge in creating this dataset is the lack of hyperspectral lunar data within the spectral range of UCIS-Moon, 0.6 to 3.6 μm. Previous missions that have collected near-IR hyperspectral images of the moon, such as M^3, do not extend past 3.0 μm. So, it was necessary to create and produce a method to realistically extrapolate a data set to 3.6 μm. The Apollo missions returned several lunar soils and other relevant lunar studies have produced lunar simulant soils that can be studied *in situ*. These samples have been spectrally characterized to wavelengths exceeding those which characterized the lunar surface from orbit.

One example is the RELAB data set, which is a laboratory with bidirectional spectrometers that collect high precision reflectance data at high spectral resolution and range. In order to produce a data set with an extended spectral range, we take advantage of sample statistics and these laboratory data sets. We use M^3 data from 0.55 to 2.8 µm and RELAB data from 1.8 to 3.75 µm to condition and create the extrapolated spectral region (2.85 to 3.75 µm) from existing M^3 pixels.

4.2.2.1 Choosing relevant M^3 scenes

First, we parsed through M^3 flight lines to find files that include lunar features of particular mineralogical interest (Table 4.2). Features on the Moon with relative mineralogy to the science objectives of UCIS-Moon were chosen to be included. The lunar feature, identified mineralogy, relevant literature citation, M^3 file ID and the particular block of pixels within each scene where the feature appears are included in Table 4.2. An example of a pixel and pixel block are shown in Figure 4.3. Using these sets of pixels, we created a dataset that is representative of interesting lunar mineralogy relative to UCIS-Moon.
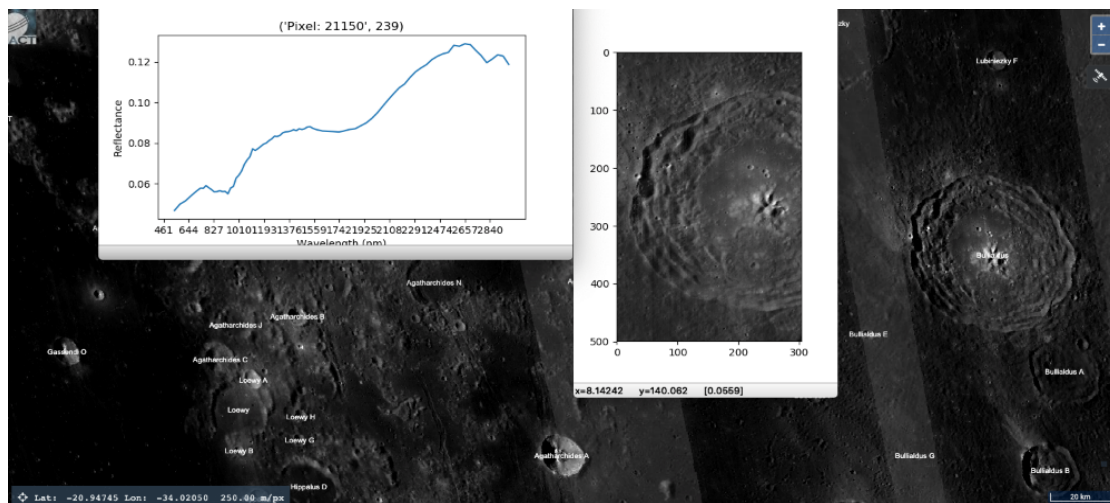
Figure 4.3: An example of a pixel taken from an M³ scene covering Bullialdus Crater. The background image is from LROC QuickMaps showing the feature on the lunar surface relative to other features.

M³ data, available on the PDS, has three distinct data products; L0: raw instrument data, L1b: calibrated radiance and backplanes, and L2: reflectance (including I/F calculation, thermal emission correction (Clark et al. 2011), photometric correction and a statistical polisher (Lundeen et al., 2011). The dataset that we aim to create simulates data collected from UCIS-Moon shortly after it is collected and converted to I/F. So, we used M³ PDS L1b files in our analysis and performed the I/F calculation described in the M³ data tutorial to convert from L1b to L2, as follows,

$$\frac{I}{F} = \frac{L_{1b} \times \pi}{\frac{L_{Sun}}{d^2}}$$

Eq. 4.5

where L_{1b} refers to the L1b radiance spectrum from M³ found in the PDS, L_{Sun} is the solar irradiance spectrum available on the PDS, and d is the mean distance from the Moon to the Sun for a given scene. The mean Moon-Sun distance for the scene is available in the backplane L1b files.

4.2.2.2 Thermally correcting M³ data prior to extrapolation

Before we were able to compare these spectra with a laboratory spectral data base extending into the spectral range of interest, we thermally corrected the M³ data using the empirical thermal correction method described in Li and Miliken (2016). Reflectance spectra collected from the lunar surface not only includes solar reflected light, but also thermally emitted light in certain wavelengths. The thermal effects do not play a significant role at wavelengths shorter than 1.5 μm but play a rather significant role in longer wavelength regions. So, it is required that the thermal

component is removed before comparing with laboratory collected spectra (Figure 4.7). Once the

thermal component of the M^3 data was removed, we moved forward in extrapolating the spectra to

3.75 μm.

Table 4.2: Lunar features with their associated composition discussed in the literature reference, M^3 file ID, and pixel block used in the compilation of our dataset.

Lunar Feature	Mineral	Publication	M^3 File name	Pixel Block #'s
Aristarchus Crater	Olivine, chrome spinel, impact melt glass & pyroclasts	Mustard et al. (2011)	M3G20090209T054031	12650-13200
Copernicus Crater	Mg-Spinel & Olivine	Pieters et al. (2014); Issacson et al. (2011)	M3G20090416T122951	9000-9275
Moscoviense Basin	Mg-spinel & Olivine	Pieters et al. (2014); Isaacson et al. (2011)	M3G20090125T172601	11800-12800; 11000-11200
Bullialdus Crater	Low Ca pyroxene & OH	Klima et al. (2011)	M3G20090416T160201; M3G20090416T181121	12600-13000; 20900-21400
Ryder Crater	OH/H_2O	Pieters et al. (2011)	M3G20090125T172601	25800-26100
Goldschmidt	OH/H_2O	Cheek et al. (2011)	M3G20090206T065053	2900-3700
Goldschmidt/Anaxagoras	OH/H_2O	Cheek et al. (2011)	M3G20090609T060742	2600-3300
Karpinskiy	OH/H_2O	Cheek et al. (2011)	M3G20090623T012541	2600-3600
Apollo 15 Landing Area	OH/H_2O	Clark et al. (2011)	M3G20090608T083142	12600-13400
South Pole PSR (e.g. Shackleton)	OH/H_2O	Zuber et al. (2012)	M3G20090131T112714; M3G20090201T125453	20400-23841;

4.2.2.3 Using RELAB to extrapolate M³ spectra to 3.75 µm

Next, we calculated the extrapolation using our knowledge of the joint distribution, i.e.

spectra encompassing the entire spectral region from 0.55 to 3.75 µm,

$$Joint: P(X,Y) = P(X)P(Y|X = x) \qquad\qquad \text{Eq. 4.6}$$

$$Conditional: P(Y|X = x) = \frac{P(X,Y)}{P(X)} \qquad\qquad \text{Eq. 4.7}$$

where X is the reflectance at shorter, known (1.8 to 2.75 µm), wavelengths and Y is the reflectance

at longer, unknown (2.8 to 3.75 µm), wavelengths. The conditional distribution (Eq. 4.7) describes

the M³ data that is extrapolated into the spectral range of interest. As noted from Eqs. 4.6 & 4.7,

the conditional is calculated using knowledge of the joint distribution. Since there is not substantial

data of the lunar surface in the region from 3.0 to 3.6 µm, we turn to laboratory spectra to

understand this joint distribution.

RELAB is a spectroscopy facility supported by Keck/NASA that, in part, supports the

measurement of lunar simulant soils and lunar soil samples returned from the Apollo missions by

NASA funded scientists. We described the joint distribution of reflectance at various wavelengths

using data collected with the near and mid-infrared spectrometer, extending from 0.3 to 25 µm.

We used the 1.8 to 3.75 µm section of these spectra in defining the joint distribution (Figure 4).

Using the RELAB (Table 4.3) and the M³ (Table 4.2) data, we extrapolated reflectance into the

spectral region of interest. For the purpose of onboard strategies relevant to UCIS-Moon, the data

is presented in I/F (Eq. 4.5).
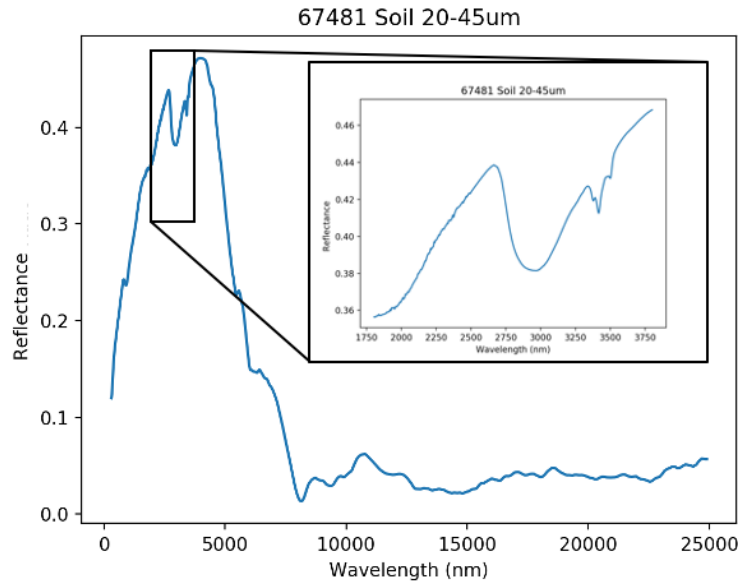
Figure 4.4: An example of a full spectrum from the RELAB database with an inset of the wavelength range used in describing the joint distribution.

Table 4.3: List of RELAB spectra used in describing the joint distribution of reflectance in the wavelength range 0.55 to 3.75 μm.

Spectrum ID	Sample ID	Spectrometer Code	Start (nm)	Stop (nm)	Resolution (nm)	Atmosphere	Date ▼	Release Date
LALR57	LR-CMP-057	BD-VNIR+BC-FTIR1	300	24923	8.0	Ambient+Dry	3-Sep-99	3-Sep-02
LBLR57	LR-CMP-057	BD-VNIR+BC-FTIR1	300	24923	8.0	Ambient+Dry	3-Sep-99	3-Sep-02
LALR58	LR-CMP-058	BD-VNIR+BC-FTIR1	300	24923	8.0	Ambient+Dry	3-Sep-99	3-Sep-02
LBLR58	LR-CMP-058	BD-VNIR+BC-FTIR1	300	24923	8.0	Ambient+Dry	3-Sep-99	3-Sep-02
LALR59	LR-CMP-059	BD-VNIR+BC-FTIR1	300	24923	8.0	Ambient+Dry	3-Sep-99	3-Sep-02
LBLR59	LR-CMP-059	BD-VNIR+BC-FTIR1	300	24923	8.0	Ambient+Dry	3-Sep-99	3-Sep-02

LALR60	LR-CMP-060	BD-VNIR+BC-FTIR1	300	24923	8.0	Ambient+Dry	3-Sep-99	3-Sep-02
LBLR60	LR-CMP-060	BD-VNIR+BC-FTIR1	300	24923	8.0	Ambient+Dry	3-Sep-99	3-Sep-02
LALX02	LX-CMP-002	BD-VNIR+BC-FTIR1	300	25920	9.0	Ambient+Dry	10-Sep-96	31-Dec-00
LALS28X	LS-CMP-028	BD-VNIR+BC-FTIR1	300	25920	9.0	Ambient+Dry	11-Sep-96	31-Dec-00
LALS28G	LS-CMP-028-A	BD-VNIR+BC-FTIR1	300	25920	9.0	Ambient+Dry	11-Sep-96	31-Dec-00
LALX03	LX-CMP-003	BD-VNIR+BC-FTIR1	300	25920	9.0	Ambient+Dry	11-Sep-96	31-Dec-00
LALX04	LX-CMP-004	BD-VNIR+BC-FTIR1	300	25920	9.0	Ambient+Dry	11-Sep-96	31-Dec-00
LBLS28X	LS-CMP-028	BD-VNIR+BC-FTIR1	300	25920	9.0	Ambient+Dry	18-Sep-96	31-Dec-00
LBLS28G	LS-CMP-028-A	BD-VNIR+BC-FTIR1	300	25920	9.0	Ambient+Dry	18-Sep-96	31-Dec-00
LBLX03	LX-CMP-003	BD-VNIR+BC-FTIR1	300	25920	9.0	Ambient+Dry	18-Sep-96	31-Dec-00
LBLX04	LX-CMP-004	BD-VNIR+BC-FTIR1	300	25920	9.0	Ambient+Dry	18-Sep-96	31-Dec-00
LALX05	LX-CMP-005	BD-VNIR+BC-FTIR1	300	25920	9.0	Ambient+Dry	18-Sep-96	31-Dec-00
LALX06	LX-CMP-006	BD-VNIR+BC-FTIR1	300	25920	9.0	Ambient+Dry	18-Sep-96	31-Dec-00
LALX07	LX-CMP-007	BD-VNIR+BC-FTIR1	300	25920	9.0	Ambient+Dry	19-Sep-96	31-Dec-00
LALX08	LX-CMP-008	BD-VNIR+BC-FTIR1	300	25920	9.0	Ambient+Dry	19-Sep-96	31-Dec-00
LALX09	LX-CMP-009	BD-VNIR+BC-FTIR1	300	25920	9.0	Ambient+Dry	21-Sep-96	31-Dec-00
LALX10	LX-CMP-010	BD-VNIR+BC-FTIR1	300	25920	9.0	Ambient+Dry	21-Sep-96	31-Dec-00
LALX11	LX-CMP-011	BD-VNIR+BC-FTIR1	300	25920	9.0	Ambient+Dry	21-Sep-96	31-Dec-00
N2LS17	LS-CMP-017	BC-FTIR1	1800	25920	9.0	Dry air	30-Jun-92	31-Dec-00
N2LS30	LS-CMP-030	BC-FTIR1	900	25920	9.0	Dry air	30-Jun-92	31-Dec-00
N2LS31	LS-CMP-031	BC-FTIR1	900	25920	9.0	Dry air	30-Jun-92	31-Dec-00

N2LS32	LS-CMP-032	BC-FTIR1	900	25920	9.0	Dry air	30-Jun-92	31-Dec-00
N2LS33	LS-CMP-033	BC-FTIR1	900	25920	9.0	Dry air	30-Jun-92	31-Dec-00
N1LS17	LS-CMP-017	BC-FTIR1	1800	25920	9.0	Dry air	1-Jul-92	31-Dec-00
N4LS17	LS-CMP-017	BC-FTIR1	1800	25920	9.0	Dry air	1-Jul-92	31-Dec-00
N1LS30	LS-CMP-030	BC-FTIR1	1800	25920	9.0	Dry air	1-Jul-92	31-Dec-00
N4LS30	LS-CMP-030	BC-FTIR1	1800	25920	9.0	Dry air	1-Jul-92	31-Dec-00
N1LS31	LS-CMP-031	BC-FTIR1	1800	25920	9.0	Dry air	1-Jul-92	31-Dec-00
N4LS31	LS-CMP-031	BC-FTIR1	1800	25920	9.0	Dry air	1-Jul-92	31-Dec-00
N1LS32	LS-CMP-032	BC-FTIR1	1800	25920	9.0	Dry air	1-Jul-92	31-Dec-00
N4LS32	LS-CMP-032	BC-FTIR1	1800	25920	9.0	Dry air	1-Jul-92	31-Dec-00
N1LS33	LS-CMP-033	BC-FTIR1	1800	25920	9.0	Dry air	1-Jul-92	31 Dec-00
N4LS33	LS-CMP-033	BC-FTIR1	1800	25920	9.0	Dry air	1-Jul-92	31-Dec-00

The RELAB data in the range of interest have obvious terrestrial absorption features indicative of hydration and organics due to contamination around 2.8 and 3.4 μm, respectively (Figure 4.4). The band depth of these features is not realistic for what we would expect in lunar data and were adjusted as such. This was conducted by calculating the weighted average between a Gaussian smoothed curve of the spectrum and a convex hull. The convex hull was weighted heavier with respect to the smoothed spectrum with the intent of eliminating absorption features. The weighted average of the two curves was then used to define the joint distribution of reflectance in the spectral range from 1.8 to 3.75 μm (Figure 4.5).
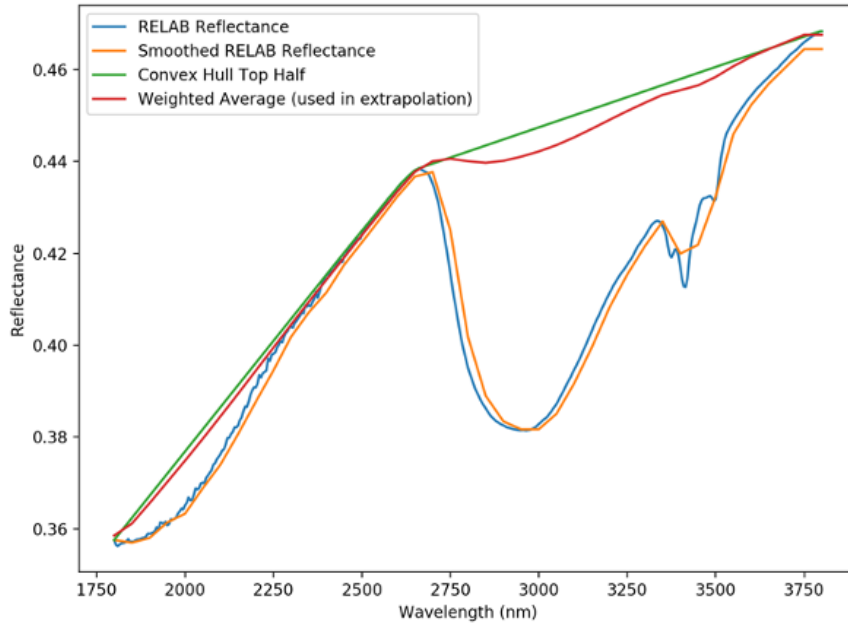
Figure 4.5: An example of a RELAB spectrum from 1800 to 3750 nm including the raw data (blue), smoothed curve (orange), calculated convex hull (green), and the weighted average between the two calculated curves (red). The curve labeled weighted average (red) was used in fitting the joint distribution.

The calculation of the joint in practice means fitting multivariate Gaussian distributions to the RELAB data. Gaussian distributions are defined by their mean and standard deviation, and in the multivariate case, the covariance between each variable i.e. the covariance matrix. The joint distribution describing reflectance in the shorter and longer wavelength ranges considers each wavelength band as a variable. That is, the covariance matrix is of size shorter wavelengths x longer wavelengths. In this particular experiment, we define the shorter wavelength range as 1.80 µm to 2.775 µm and the longer wavelength range as 2.776 µm to 3.750 µm with 5 nm spectral resolution. We use the submatrix components of the joint covariance matrix, calculated using the RELAB data (Figure 4.5), to calculate the mean and covariance of the conditional distribution, when the joint is partitioned and described as follows,

61

$$Entire\ Range = \begin{bmatrix} SW \\ LW \end{bmatrix} of\ size \begin{bmatrix} 195 \\ 195 \end{bmatrix} \qquad \text{Eq. 4.8}$$

with parameters μ and Σ defined as,

$$\mu = \begin{bmatrix} \mu_{SW} \\ \mu_{LW} \end{bmatrix} of\ size \begin{bmatrix} 195 \\ 195 \end{bmatrix} \qquad \text{Eq. 4.9}$$

$$\Sigma = \begin{bmatrix} \Sigma_{SWSW} & \Sigma_{SWLW} \\ \Sigma_{LWSW} & \Sigma_{LWLW} \end{bmatrix} of\ size \begin{bmatrix} 195x195 & 195x195 \\ 195x195 & 195x195 \end{bmatrix}. \qquad \text{Eq. 4.10}$$

Then the conditional distribution of LW given that SW is equal to known M^3 reflectance values is fit to a multivariate Gaussian distribution, i.e. $(LW|SW = M^3) \sim N(\bar{\mu}, \bar{\Sigma})$, where

$$\bar{\mu} = \mu_2 + \Sigma_{SWLW}\Sigma_{LWLW}^{-1}(M^3 - \mu_1) \qquad \text{Eq. 4.11}$$

$$\bar{\Sigma} = \Sigma_{SWSW} - \Sigma_{SWLW}\Sigma_{LWLW}^{-1}\Sigma_{LWSW}. \qquad \text{Eq. 4.12}$$

Completing this calculation produced a multivariate Gaussian distribution of the longer wavelength reflectance values based on the measured reflectance values from M^3 and provides a realistic extrapolation of previously collected lunar data to 3.75 μm (Figure 4.8). Next, we use more RELAB spectra to include absorption features of particular interest in the extrapolated data set.

4.2.2.4 Adding absorption features to the extrapolation

Table 4.4: List of RELAB spectra used in adding absorption features in the wavelength range 0.55 to 3.75 μm.

Spectrum ID	Sample ID	Feature Present	Spectrometer Code	Start (nm)	Stop (nm)	Resolution (nm)	Atmosphere	Date ▾	Release Date
LALR14	LR-CMP-014	Olivine	BD-VNIR+BC-FTIR1	300	25920	9.0	Ambient+Dry	3-Nov-97	31-Dec-00
LASP19	SP-EAC-019	Spinel	BD-VNIR+BC-FTIR1	300	25920	9.0	Ambient+Dry	3-Nov-99	31-Dec-03
BKR1LR112	LR-CMP-112	Mature Regolith	BD-VNIR+BCF-FTIR2	300	25050	4.0	Ambient+Dry	1-Feb-03	1-Feb-06
BKR1LR121	LR-CMP-121	Pyroxene	BD-VNIR+BCF-FTIR2	300	25050	4.0	Ambient+Dry	2-Oct-03	2-Oct-06
BKR1JB708	JB-JLB-708	Hematite	BD-VNIR+BCF-FTIR2	320	99719	4.0	Ambient+Dry	31-Mar-06	31-Mar-09

UCIS-Moon is interested in detecting, if present, the minerals hematite, pyroxene, olivine and Mg-spinel as well as H_2O mineral hydration, molecules, ice, and OH. All of the RELAB spectra include the aforementioned absorption features from OH and organics at 2.8 μm and 3.4 μm, respectively. Table 4.4 includes the particular RELAB spectra used in adding absorption features to the extrapolated data set (Figure 4.6). We created a convex hull around the RELAB spectra and divided one by the other to get a spectrum with a continuum at one. Next, we subtracted one, multiplied by the 0.25 to shrink the depth of the features, and added back one before multiplying this spectrum by the extrapolated M^3 spectrum. In order to characterize the ability of the prioritization algorithms to find and select spectra with these features successfully, we included 20 spectra with each feature. The description and success of these algorithms can be found in section 4.2.3 and section 4.3.2, respectively.
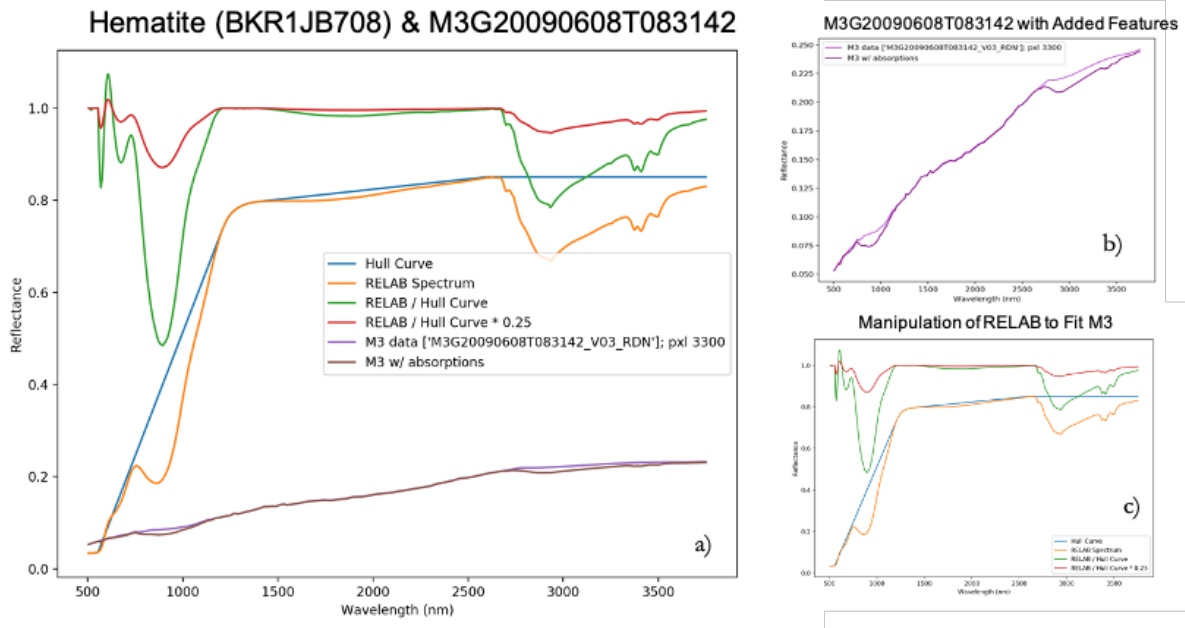
Figure 4.6: A figure showing an example RELAB spectrum (BKR1JB708), a pixel from the M3G20090608T083142 M3 scene, and the steps taken to reach the final product in reflectance values; a) all spectra used in the process of adding absorption features to the extrapolated spectrum, b) the extrapolated spectrum overlain with the extrapolated spectrum with absorption features, and c) the RELAB example spectrum with absorption features of interest and the subsequent steps used to create the spectra in b).

4.2.2.5 Adding a lunar simulant thermal component to the extrapolation

As described in the thermal correction used at the beginning of the extrapolation process, the radiation at the satellite is composed of a thermal and non-thermal component as follows (Hapke, 2012: equation 15.31),

$$L_{sat} = L_{non-therm} + L_{therm,} \hspace{3cm} \text{Eq. 13}$$

where L_{sat} is the radiation at the satellite, $L_{non\text{-}therm}$ is the non-thermal radiance component, and L_{therm} is the thermal radiance component. I/F, described in Eq. 4.5, is calculated using the radiance at the satellite and the solar radiance, J/π where J is the solar irradiance. The total lunar thermal

component is described as the blackbody radiation times the emissivity. Kirchoff's law, $\varepsilon = 1 - R_{BiDr}$, where ε is emissivity and R_{BiDr} is bidirectional reflectance $(R_{I/F} * \cos(i))$, is assumed to be true in this process. This gives,

$$L_{sat} = \frac{J}{\pi} * R_{BiDr} + L_{BB}(T) * (1 - R_{BiDr}).$$ Eq. 4.14

Li and Miliken (2016) further describes the thermal correction process using this equation. Ultimately, to add the thermal component into the extrapolated dataset, we simply add $L_{BB}(T) * (1 - R_{BiDr})$ to the extrapolated data after converting it to radiance, $\frac{J}{\pi} * R_{I/F}$. For our specific purpose of UCIS-Moon, where the data being input into the thermal correction and prioritization algorithms will be converted to I/F, we also translate our extrapolated dataset with added absorption features and thermal component to I/F using Eq. 4.5 (Figure 4.7).

['M3G20090608T083142_V03_RDN']

Legend:
- L1B M3 pxl 615600
- Thermally Correctred M3 Smooth
- Extrapolation w absp ft w/o Thermal Component
- Thermally Correctred M3 pxl 615600
- Extrapolation w Thermal Comopnent; T = 363.819849
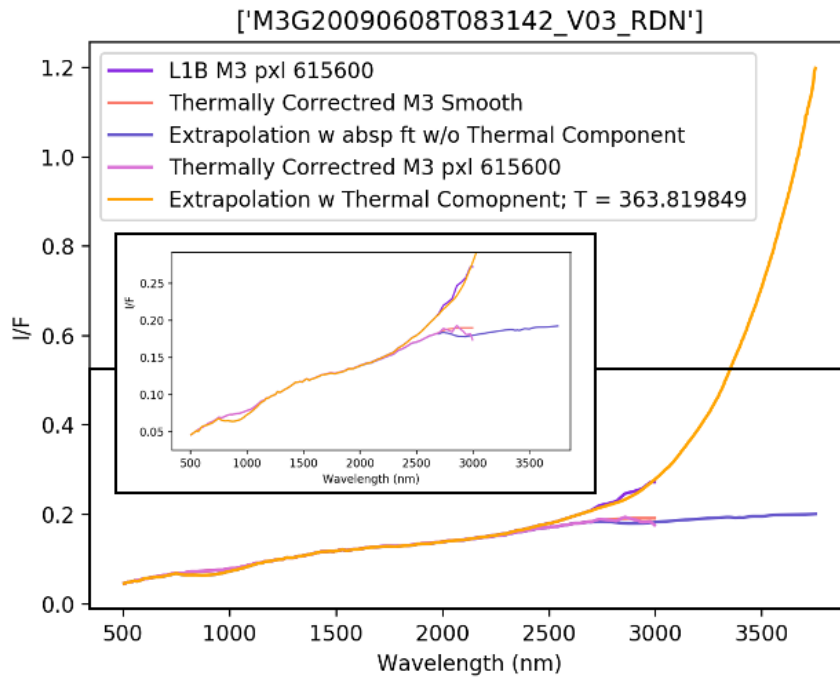
Figure 4.7: A pixel from the M3G20090608T083142 M3 scene with I/F values extrapolated to 3.75 μm, added absorption features, and thermal component using the described technique.

4.2.3 Thermally correcting the extrapolated dataset

We use the same process described in the previous subsection and Li and Miliken (2016) to find the temperature of each pixel, compute, and remove the thermal component. Removing this thermal component reveals absorption features in the longer wavelengths dominated by thermal, such as water, OH and organics. Thus, it is necessary to remove the thermal component before analyzing for absorption features of interest.

We encountered two sensitivities when calculating the thermal component in the extrapolated data (Figure 8). The first sensitivity lies in using the I/F at 1.55 μm to ultimately predict the temperature, as described in Li and Miliken (2016). We found that if the I/F value is changed by 0.0002, the resulting temperature is changed by 0.217 K, which can make a significant difference in predicting the thermal component for each spectrum (Li et al., 2017; Bandfield et al., 2018). This slight change or error in predicting the temperature led to another issue in the sensitive calculation of the thermal component while assuming Kirchoff's Law, $\varepsilon + R = 1$ (where ε is emissivity and is bi-directional reflectance). The sensitivity is seen when using the satellite equation (Eq. 4.13, 4.14) to solve for the non-thermal component,

$$R_{BiDr} = \frac{L_{sat} - L_{BB}}{J_{/(d^2 * \pi)} - L_{BB}}.$$ Eq. 4.15

In Eq. 4.15, the denominator will approach 0 at a particular wavelength as the solar spectrum and the black body radiation values converge (Figure 4.8a). The wavelength of this convergence depends on the predicted temperature used in calculating L_{BB} and the solar spectrum, which in this

case is collected from the Moon. This sensitivity was not seen in the extrapolation process, although it was encountered in the thermal component removal. Since we added absorption features to our extrapolated spectra, the I/F at 1.55 µm is slightly different from the M³ data used to predict the temperature and condition the extrapolation. Thus, the prediction of the temperature using the extrapolated data with a thermal component and added absorption features is incorrect by 0.5 K and causes a singularity in the calculation of the non-thermal component as the values in the denominator converge. For one of our spectra, this is encountered at approximately 3.5 µm.
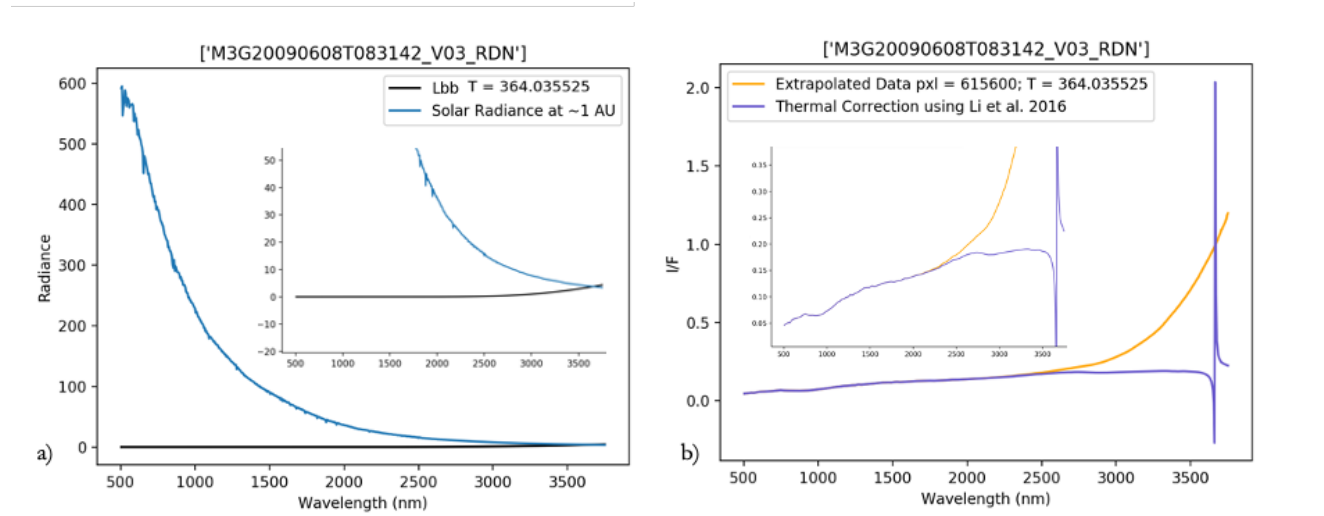
Figure 4.8: The sensitivities in the empirical calculation of the thermal component in lunar spectra; a) the denominator in Eq. 4.15, showed as they approach the same values and b) the result of using Eq. 4.15 to calculate the non-thermal component in a lunar spectrum when the denominator approaches and reaches 0.

4.3 Results & Discussion

4.3.1 The Finalized Extrapolated Dataset Simulant of Lunar Imaging Spectra from 0.5 to 3.75 µm

An example of a thermally corrected extrapolated pixel with absorption features is shown in Figure 4.9. The values at wavelengths shorter than 2.775 µm are directly M³-collected values

while values at wavelengths longer than 2.776 μm are drawn from the computed, conditional

multivariate Gaussian distributions.
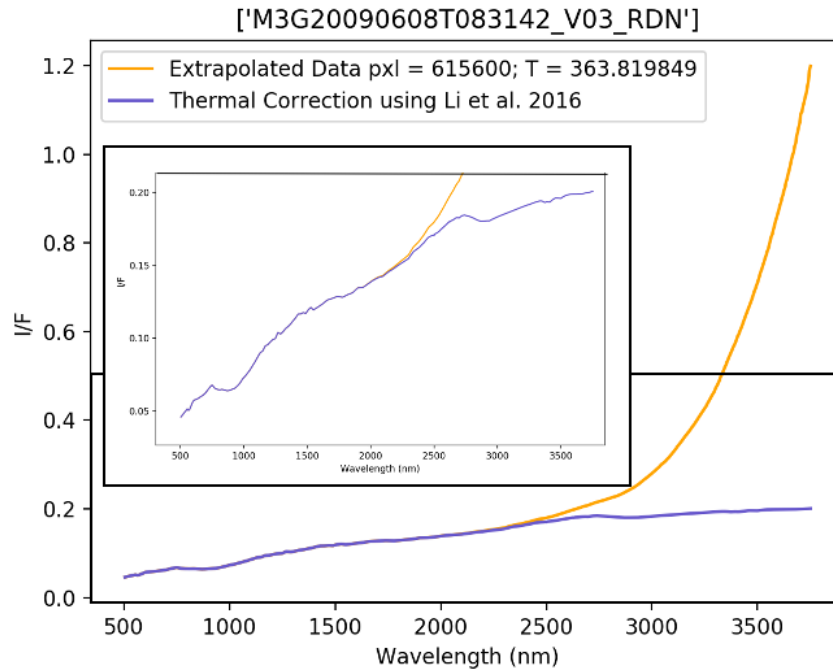
Figure 4.9: A pixel from our extrapolated dataset thermally corrected prior to being used in testing the prioritization algorithms. The M3 spectrum used in the extrapolation process is shown with (orange) and without (purple) its thermal component.

4.3.2 Success of Possible Onboard Prioritization Algorithms

We used the simulated dataset described above to test the prioritization algorithms. We

took a sample size of 200 spectra, 100 of which included added absorption features from Table 4.4

and 100 of which included raw spectra with no added absorption features. Table 4.5 shows the

results from our test. The CIBR algorithm proved to be the most accurate, with an 91 % success

rate of classifying spectra with absorption features of interest, or true positive rate. This process

incorrectly classified 13 % of the data, labeling one of the 20 spectra with no added features as a

spectrum of interest, i.e. the false positive rate while producing 10 false negatives. From our

experiment, a CIBR method onboard would reduce the downlink of an imaging spectrometer on or near the lunar surface by 48 %.

The RX algorithm is a less rigorous approach that classified 89% of the spectra with added features at the cost of misclassifying 65% of the data with no added features. This method produced 11 false negatives and would reduce onboard data by 23.5 %. But it is important to note that a imaging spectrometer mission to the lunar surface with the intent to study volatiles and discover interesting mineralogy would likely choose to include the RX detection method, since the bands of interests would not be known. Combining the two process showed a promising result with 8 false negatives, 90 % true positive rate, and an overall data reduction of 22 %.

Depending on the mission criteria, the definition of a classification changes. Mission criteria that would change this sensitivity mainly include site statistics and the defined compression rate. The CIBR threshold can be adjusted to match these criteria. For example, Lucey et al. (2014) conducted a comprehensive study of lunar craters comprising 8184 spectra where only 13 were determined to have mineralogical anomalies. In terms of the definitions used in this study, 0.15 % of the total dataset were interesting spectra. Using both methods, about 6300 spectra would be prioritized for download but only 11 of them would be true positives. But using CIBR would reduce the downlink to about 4256 spectra and include 12 true positives. This shows that the CIBR method best compresses the total data for downlink while preserving almost all of the scientifically valuable spectra.

Table 4.5: Results of the prioritization tests using the thermally corrected extrapolated data set. We use a CIBR threshold of 0.93, as determined from studying the false and true positive rates. The RX anomaly uses neighboring 20 bands to the band of interest, 10 on each side.

Method	Input Spectra w/ Features of Interest	Input Spectra w/o Features of Interest	Prioritized Spectra	Misclassified Spectra	Lost Spectra of Interest
CIBR	100	100	104	13	10
RX	100	100	153	64	11
Both	100	100	156	64	8

Method	**Correctly Prioritized Data** (% of Data **w** Features)	**Incorrectly Prioritized Data** (% of Data **w/o** Features)	**Prioritized for Downlink** (% of **Total** Data)	Reduction in Downlink (% of **Total** Data)
CIBR	91 %	13 %	52 %	48 %
RX	89 %	64 %	76.5 %	23.5 %
Both	90 %	64 %	78 %	22 %

4.3 Conclusion

Onboard prioritization is a simple solution to data optimization in combating larger data sets outgrowing the available downlink bandwidth. In our test, we decreased overall data volume by prioritizing scientifically relevant spectra. In particular, we reduced a test dataset by 22 % while correctly classifying 90 % of the scientifically valuable spectra using two spectral prioritization methods, namely CIBR and RX anomaly detection. These methods combined are more accurate for classification, saving the most relevant data with minimal loss.

To test these methods, we created an extrapolated dataset simulant of the lunar surface from 0.5 to 3.75 µm, using M^3 and RELAB. This dataset is relevant to the lunar science community since the spectral characteristics of the Moon in the spectral range from 0.5 to 3.75 µm is essential to test the onboard processing algorithms proposed for UCIS-Moon and other instruments with the intent to study the lunar surface past 3.0 µm.

Conclusion

In the course of this dissertation, I have approached three main topics essential to planetary missions. This includes the development of instrumentation, the testing and qualification of instrumentation by relating specific instrumentation to the scientific needs of a particular mission, and data optimization. Two different types of remote spectroscopic techniques were discussed, namely Raman spectroscopy and hyperspectral imaging spectroscopy. Both types of spectroscopy are relevant to the planetary science community for future missions. This dissertation provides substantial research for the advancement and innovation of remote spectroscopic techniques for planetary exploration.

References

Abbas, O. and Schulze-Makuch, D. "Acetylene-Based Pathways for Prebiotic Evolution on Titan", Proc 2nd European Workshop on Exo/Astrobiology, Graz, Austria, Sept 16-19, 2002.

Acosta-Maeda, T. E., Misra, A. K., Muzangwa, L. G., Berlanga, G., Muchow, D., Porter, J., Sharma, S. K. "Remote Raman Measurements of Minerals, Organics, and Inorganics at 430 m Range." Appl. Opt. 2016. 55 (36): 10283-10289. doi:10.1364/ao.55.010283.

Acosta-Maeda, T. E., Misra, A. K., Muzangwa, L. G., Berlanga, G., Sharma, S. K., Abedin, M. N. "Stand-off Detection of Amino Acids and Nucleic Bases Using a Compact Instrument as a Tool for Search for Life." Lidar Remote Sensing for Environmental Monitoring XVI, Proc. SPIE 2018: 10779:107790K/1-10. doi:10.1117/12.2324827.

Angel, M. S., Gomer, N. R., Sharma, S. K., and Mckay, C. "Remote Raman Spectroscopy for Planetary Exploration: A Review." Appl. Spectrosc. 2012. 66(2): 137-150.

Bandfield, J. L., Poston, M. J., Klima, R. L., & Edwards, C. S. (2018). Widespread distribution of OH/H2O on the lunar surface inferred from spectral data. Nat Geosci, 11, 173-177. doi:10.1038/s41561-018-0065-0

Beyssac, O. (2020). New Trends in Raman Spectroscopy: From High-Resolution Geochemistry to Planetary Exploration. Elements, 16(2), 117-122. doi:10.2138/gselements.16.2.117

Blacksberg, J., Alerstam, E., Maruyama, Y., Cochrane, C. J., and Rossman, G. R. "Miniaturized time-resolved Raman spectrometer for planetary science based on a fast single photon avalanche diode detector array," Appl. Opt. 2016. 55: 739–748.

Blaney, D. L., Clark, R., Dalton, J. B., Davies, A. G., Green, R., Hedman, M., . . . Strohbehn, K. (2015). Mapping Imaging Spectrometer for Europa (MISE). EPSC Abstracts, 10.

Boardman, J. W., & Kruse, F. A. (2011). Analysis of Imaging Spectrometer Data Using N-Dimensional Geometry and a Mixture-Tuned Matched Filtering Approach. IEEE Transactions on Geoscience and Remote Sensing, 49(11), 4138-4152. doi:10.1109/tgrs.2011.2161585

Boardman, J. W., Pieters, C. M., Green, R. O., Lundeen, S. R., Varanasi, P., Nettles, J., . . . Taylor, L. A. (2011). Measuring moonlight: An overview of the spatial properties, lunar coverage, selenolocation, and related Level 1B products of the Moon Mineralogy Mapper. Journal of Geophysical Research, 116. doi:10.1029/2010je003730

Böttger, U., Bulat, S. A., Hanke, F., Pavlov, S. G., Greiner-Bär, M., & Hübers, H. W. Identification of inorganic and organic inclusions in the subglacial Antarctic Lake Vostok ice with Raman spectroscopy. Journal of Raman Spectroscopy 48, 1503-1508 (2017).

Brigiano, F. S., Jeanvoine, Y., Largo, A., and Spezia, R. "The Formation of Urea in Space. I. Ion-Molecule, Neutral-Neutral, and Radical Gas-Phase Reactions", A &A. 2018. 610: A26/ 1-15

Brown, M. E., Hand K. P. Salts and Radiation Products on the Surface of Europa. The Astronomical Journal 145, 110/1-7 (2013).

Cai, Y. Q., Mao, H. K., Chow, P. C., Tse, J. S., Ma, Y., Patchkovskii, S., Shu, J. F., Struzhkin, V., Hemley, R. J., Ishii, H., Chen, C. C., Jarrige, I., Chen, C. T., Shieh, S. R., Huang, E. P., and Kao, C. C. Ordering of hydrogen bonds in high-pressure low-temperature H2O. Phys Rev Lett 94, 025502 (2005).

Carlson, R. & Calvin, W. & Dalton, James & Hansen, G. & Hudson, Reggie & Johnson, R. & Mccord, Thomas & Moore, M. Europa's Surface Composition. Europa. 283-. (2009).

Carlson, R. W., Anderson, M. S., Johnson, R. E., Schulman, M. B., & Yavrouian, A. H. (2002). Sulfuric Acid Production on Europa: The Radiolysis of Sulfur in Water Ice. Icarus, 157(2), 456-463. (2002). doi:10.1006/icar.2002.6858

Carlson, R. W., Anderson, M. S., Johnson, R. E., Smythe, W. D., Hendrix, A. R., Barth, C. A., . . . Matson, D. L. Hydrogen Peroxide on the Surface of Europa. Science, 283(5310), 2062-2064. (1999).

Carter, J., Poulet, F., Murchie, S., & Bibring, J. P. (2013). Automated processing of planetary hyperspectral datasets for the extraction of weak mineral signatures and applications to CRISM observations of hydrated silicates on Mars. Planetary and Space Science, 76, 53-67. doi:10.1016/j.pss.2012.11.007

Cheek, L. C., Pieters, C. M., Boardman, J. W., Clark, R. N., Combe, J. P., Head, J. W., . . . Taylor, L. A. (2011). Goldschmidt crater and the Moon's north polar region: Results from the Moon Mineralogy Mapper (M3). Journal of Geophysical Research, 116. doi:10.1029/2010je003702

Clark, R. N., & Swayze, G. A. (1995). Mapping Minerals, Vegetation, Amorphous Materials, Environmental Materials, Vegetation, Water Ice and Snow and Other Materials: The USGS Tricorder Algorithm. JPL.

Clark, R. N., Gallagher, A. J., & Swayze, G. A. (1990). Material absorption band depth mapping of imaging spectrometer data using a complete band shape least-squares fit with library reference spectra. In Proceedings of the Second Airborne Visible/Infrared Imaging Spectrometer (AVIRIS) Workshop (Vol. 90, pp. 176-186). JPL Publication 90-54.

Clark, R. N., Pieters, C. M., Green, R. O., Boardman, J. W., & Petro, N. E. (2011). Thermal removal from near-infrared imaging spectroscopy data of the Moon. Journal of Geophysical Research, 116. doi:10.1029/2010je003751

Clark, R. N., Swayze, G. A., Koch, C., & Ager, C. (1992). Mapping Vegetation Types with the Multiple Spectral Feature Mapping Algorithm in Both Emission and Absorption. USGS.

Creamer, J. S., Mora, M. F., Willis, P. A. Enhanced Resolution of Chiral Amino Acids with Capillary Electrophoresis for Biosignature Detection in Extraterrestrial Samples. Anal Chem 89, 1329-1337 (2017).

Creamer, J. S., Mora, M. F., Willis, P. A. Stability of reagents used for chiral amino acid analysis during spaceflight missions in high-radiation environments. Electrophoresis 39, 2864-2871 (2018).

Culka, A., Jehličˇka, J., "Raman microspectrometric Investigation of Urea in Calcite and Gypsum Powder Matrices". J. Raman Spectrosc. 2010. 41(12): 1743–1747.

Culka, A., Jehlicka, J., Edwards, H. G. "Acquisition of Raman Spectra of Amino acids using portable instruments: Outdoor measurements and comparison." Spectrochim. Acta, Part A. 2010. 77(5): 978–983. doi:10.1016/j.saa.2010.08.034.

Dalton III, J. B., Shirley, J. H., and Kamp, L. W. "Europa's Icy Bright Plains and Dark Linea: Exogenic and Endogenic Contributions to Composition and Surface Properties", J. Geophys. Res. 2012. 117: E03003/ 1-16.

Dalton, J. B., Cassidy, T., Paranicas, C., Shirley, J. H., Prockter, L. M., & Kamp, L. W. Exogenic controls on sulfuric acid hydrate production at the surface of Europa. Planetary and Space Science 77, 45-63 (2013).

Dalton, J. B., Prieto-Ballesteros, O., Kargel, J. S., Jamieson, C. S., Jolivet, J., & Quinn, R. (2005). Spectral comparison of heavily hydrated salts with disrupted terrains on Europa. Icarus, 177(2), 472-490. doi:10.1016/j.icarus.2005.02.023

Durickovic, I., Machetti, M., Claverie, R., Bourson, P., Chassort, J.-M. and Fontana, M. Experimental Study of NaCl Aqueous Solutions by Raman Spectroscopy: Towards a New Optical Sensor. Applied Spectroscopy 64(8), 853-857 (2010). doi: 10.1366/000370210792080984.

Ferraro, J. R., Nakamoto, K., and Brown, C. W. Introductory Raman Spectroscopy, 2nd ed. Academic Press. 2003.

Fini, G. "Applications of Raman Spectroscopy to Pharmacy," J. Raman Spectrosc. 2003. 35: 335–337.

Frost, R.L., Kristof, J., Rintoul, L., et al. "Raman Spectroscopy of Urea and Urea-Intercalated Kaolinites at 77 K". Spectrochim. Acta. Part A. 2000. 56(9): 1681–1691.

Gasda, P. J., Acosta-Maeda, T. E., Lucey, P. G., Misra, A. K., Sharma, S. K., and Taylor, G. J. "Next Generation Laser-Based Standoff Spectroscopy Techniques for Mars Exploration." Appl. Spectrosc. 2015. 69(2); 173-92.

Geissler, P. E., Greenberg, R., Hoppa, G., McEwen, A., Tufts, R., Phillips, C., Clark, B., Ockert-Bell, M., Helfenstein, P., Burns, J., Veverka, J., Sullivan, R., Greeley, R., Pappalardo, R. T., Head III, J. W., Belton, M. J. S., Denk, T. Evolution of Lineaments on Europa: Clues from Galileo Multispectral Imaging Observations. Icarus 135, 107-126 (1998).

Giambelluca, T. W., Shuai, X., Barnes, M.L., Alliss, R.J., Longman, R.J., Miura, T., Chen, Q., Frazier, A.G., Mudd, R.G., Cuo, L., and Businger, A.D. Evapotranspiration of Hawai'i. Final Report. 2014. pp. 178. [accessed 2020 June 1]; http://evapotranspiration.geography.hawaii.edu/assets/files/PDF/ET%20Project%20Final %20Report.pdf

Grasset, O., Dougherty, M.K., Coustenis, A., Bunce, E.J., Erd, C., Titov, D., Blanc, M., Coates, A., Drossart, P., Fletcher, L.N., Hussmann, H., Jaumann, R., Krupp, N., Lebreton, J.-P., Prieto-Ballesteros, O., Tortora, P., Tosi, F., Van Hoolst, T. JUpiter ICy moons Explorer (JUICE): An ESA mission to orbit Ganymede and to characterise the Jupiter system, Planetary and Space Science, 78, 1-21 (2013). https://doi.org/10.1016/j.pss.2012.12.002.

Green, A. A., Berman, M., Switzer, P., & Craig, M. D. (1988). A Transformation for Ordering Multispectral Data in Terms of Image Quality with Implications for Noise Removal. IEEE Transactions on Geoscience and Remote Sensing, 26.

Green, R. O., Pieters, C., Mouroulis, P., Eastwood, M., Boardman, J., Glavich, T., . . . Wilson, D. (2011). The Moon Mineralogy Mapper (M3) imaging spectrometer for lunar science: Instrument description, calibration, on-orbit measurements, science data calibration and on-orbit validation. Journal of Geophysical Research, 116. doi:10.1029/2011je003797

Griffith, W. P. "Raman Spectroscopy of Minerals," Nature. 1969. 224: 264–266.

Hand, K. P. and German, C. R. Exploring Ocean Worlds on Earth and Beyond. Nature Geoscience 11, 2-5 (2018).

Hand, K.P., Murray, A.E., Garvin,J., Horst, S., Brinkerhoff, W., Edgett, K., Hoehler, T., Russell, M., Rhoden, A., Yingst, R.A., German, C., Schmidt, B., Paranicas, C., Smith, D., Willis, P., Hayes, A., Ehlmann, B., Lunine, J., Templeton, A., Nealson, K., Christner, B., Cable, M., Craft, K., Pappalardo, R., and Phillips, C. Science goals, objectives, and investigations of the 2016 Europa Lander Science Definition Team Report [abstract 2492]. In 48th Lunar

and Planetary Science Conference, Lunar and Planetary Institute, Houston, LPI Contribution No: 1964. (2017).

Hanlon, E., Manoharan, R., Koo, T.W., Shafer, K., Motz, J., Fitzmaurice, M., Kramer, J., Itzkan, I., Dasari, R., and Feld, M. "Prospects For in Vivo Raman Spectroscopy," Phys. Med. Biol. 2000. 45: R1–R59.

Hapke, B. (2012). Theory of Reflectance and Emittance Spectroscopy. Cambridge University Press.

Hendrix, A. R. and Hurford, T. A., Barge, L. M., Bland, M. T., Bowman, J. S., Brinckerhoff, W., Buratti, B. J., Cable, M. L., Castillo-Rogez, J., Collins, G. C., Diniega, S., German, C. R., Hayes, A. G., Hoehler, T., Hosseini, S., Howett, C. J.A., McEwen, A. S., Neish, C. D., Neveu, M., Nordheim, T. A., Patterson, G. W., Patthoff, D. A., Phillips, C., Rhoden, A., Schmidt, B. E., Singer, K. N., Soderblom, J. M., and Vance, S. D. The NASA Roadmap to Ocean Worlds. Astrobiology,.19(1), 1-27 (2019). http://doi.org/10.1089/ast.2018.1955.

Hodyss, R., Parkinson, C. D., Johnson, P. V., Stern, J. V., Goguen, J. D., Yung, Y. L., & Kanik, I. Methanol on Enceladus. Geophysical Research Letters 36, (2009).

Horgan, B. H. , Bell III, J. F., Noe Dobrea, E. Z., Cloutis, E. A., Bailey, D. T., Craig, M. A., Roach, L. H., and Mustard, J. F. "Distribution of hydrated minerals in the North Polar Region of Mars", J. Geophys. Res. 2009. 114: E01005/1-24

Howell, S. M. & Pappalardo, R. T. Band formation and ocean-surface interaction on Europa and Ganymede. Geophysical Research Letters, 45, 4701–4709. (2018). https://doi.org/10.1029/2018GL077594.

Howell, S. M., Pappalardo, R. T. Can Earth-like plate tectonics occur in ocean world ice shells?, Icarus, Volume 322, Pages 69-79, (2019). https://doi.org/10.1016/j.icarus.2019.01.011.

Howell, S.M., Pappalardo, R.T. NASA's Europa Clipper—a mission to a potentially habitable ocean world. Nat Commun 11, 1311 (2020). https://doi.org/10.1038/s41467-020-15160-9

Isaacson, P. J., Pieters, C. M., Besse, S., Clark, R. N., Head, J. W., Klima, R. L., . . . Tompkins, S. (2011). Remote compositional analysis of lunar olivine-rich lithologies with Moon Mineralogy Mapper (M3) spectra. Journal of Geophysical Research, 116. doi:10.1029/2010je003731

Jia, X., Kivelson, M.G., Khurana, K.K., and Kurth, W. S. Evidence of a plume on Europa from Galileo magnetic and plasma wave signatures. Nat Astron 2, 459–464 (2018). https://doi.org/10.1038/s41550-018-0450-z.

Kiefert, L. and Karampelas, S. "Use of the Raman Spectrometer in Gemological Laboratories: Review," Spectrochim. Acta. Part A. 2011. 80: 119–124.

Kimura, J., Kitadai, N. Polymerization of Building Blocks of Life on Europa and Other Icy Moons. Astrobiology 15, 430-441 (2015).

Kivelson, M. G., Khurana, K. K., & Volwerk, M. (2002). The permanent and inductive magnetic moments of Ganymede. Icarus, 157(2), 507-522.

Klima, R. L., Pieters, C. M., Boardman, J. W., Green, R. O., Head, J. W., Isaacson, P. J., . . . Tompkins, S. (2011). New insights into lunar petrology: Distribution and composition of prominent low-Ca pyroxene exposures as observed by the Moon Mineralogy Mapper (M3). Journal of Geophysical Research, 116. doi:10.1029/2010je003719

Korablev, O., Gerasimov, M., Brad Dalton, J., Hand, K., Lebreton, J.-P., & Webster, C. Methods and measurements to assess physical and geochemical conditions at the surface of Europa. Advances in Space Research 48, 702-717 (2010).

Kramer, G. Y., Besse, S., Dhingra, D., Nettles, J., Klima, R., Garrick-Bethell, I., . . . McCord, T. B. (2011). M3spectral analysis of lunar swirls and the link between optical maturation and

surface hydroxyl formation at magnetic anomalies. Journal of Geophysical Research, 116. doi:10.1029/2010je003729

Li, S., & Li, L. (2011). Radiative transfer modeling for quantifying lunar surface minerals, particle size, and submicroscopic metallic Fe. Journal of Geophysical Research, 116(E9). doi:10.1029/2011je003837

Li, S., & Milliken, R. E. (2016). An empirical thermal correction model for Moon Mineralogy Mapper data constrained by laboratory spectra and Diviner temperatures. Journal of Geophysical Research: Planets, 121(10), 2081-2107. doi:10.1002/2016je005035

Li, S., Lucey, P. G., Milliken, R. E., Hayne, P. O., Fisher, E., Williams, J. P., . . . Elphic, R. C. (2018). Direct evidence of surface exposed water ice in the lunar polar regions. Proc Natl Acad Sci U S A, 115(36), 8907-8912. doi:10.1073/pnas.1802345115

Lippincott, E. R. and O'reilly, E. J. "Vibrational Spectra and Assignment of Naphthalene and Naphthalene-d-8." J. Chem. Phys. 1955. 23(2): 238–244. doi:10.1063/1.1741947.

Lorenz, R. D. Europa ocean sampling by plume flythrough: Astrobiological expectations, Icarus, Volume 267, Pages 217-219, 2016. https://doi.org/10.1016/j.icarus.2015.12.018.

Lucey, Paul G., Norman, J. A., Crites, S. T., Taylor, G. J., Hawke, B., Lemelin, M., and Melosh, H. J. A large spectral survey of small lunar craters: Implications for the composition of the lunar mantle. American Mineralogist 99, no. 11-12 (2014): 2251-2257.

Lundeen, S., Stephanie, M., and Rafael, A. Moon Mineralogy Mapper, DATA PRODUCT SOFTWARE INTERFACE SPECIFICATION Rep. (2011).

Mammone, J. F., Sharma, S. K., Nicol, M. Raman Spectra of Methanol and Ethanol at Pressures up to 100kbar. American Chemical Socierty 84, (1980).

Manolakis, Dimitris G, Ronald B Lockwood, and Thomas W Cooley. Hyperspectral Imaging Remote Sensing: Physics, Sensors, and Algorithms. Cambridge University Press, 2016. Web.

Martinez-Fria, J., Amaral, G. and Vazquez, L. "Astrobiological Significance of Minerals on Mars Surface Environment", Rev. Environ. Sci. Biotechnol. 2006. 5:219–231

Matthewman, R., Court, R. W., Crawford, I. A., Jones, A. P., Joy, K. H., & Sephton, M. A. The Moon as a Recorder of Organic Evolution in the Early Solar System: A Lunar Regolith Analog Study. Astrobiology, 15(2), 154-168. (2015). doi:10.1089/ast.2014.1217.

McCord, T. B., Hansen, G. B., Combe, J.-P., Hayne, P. Hydrated minerals on Europa's surface: An improved look from the Galileo NIMS investigation. Icarus 209, 639-650 (2010).

McCord, T. B., Taylor, L. A., Combe, J. P., Kramer, G., Pieters, C. M., Sunshine, J. M., & Clark, R. N. (2011). Sources and physical processes responsible for $OH/H2O$ in the lunar soil as revealed by the Moon Mineralogy Mapper (M3). Journal of Geophysical Research, 116. doi:10.1029/2010je003711

McCreery, R. L. "Raman Spectroscopy for Chemical Analysis," in J. D. Winefodner, Editor, Chemical Analysis, Vol. 157, pp. 420. New York, John Wiley & Sons, Inc., 2000.

McKinnon, W. B. and Zolensky, M. E. "Sulfate Content of Europa's Ocean and Shell: Evolutionary Considerations and Some Geological and Astrobiological Implications," Astrobiology. 2003(3): 879–897.

Misra, A. K., Acosta-Maeda, T. E., Porter, J. N., Berlanga, G., Muchow, D., Sharma, S. K., and Chee, B. "A Two Components Approach for Long Range Remote Raman and Laser-Induced Breakdown (LIBS) Spectroscopy Using Low Laser Pulse Energy." Appl. Spectrosc. 2018. 73(3): 320-328.

Misra, A. K., Acosta-Maeda, T. E., Porter, J. N., Egan, M. J., Sandford, M. W., Oyama, T., & Zhou, J. "Remote Raman Detection of Chemicals from 1752 m During Afternoon Daylight," Appl. Spectrosc. 2020. 74(2): 233-240 doi:10.1177/0003702819875437

Misra, A. K., Sharma, S. K., Acosta, T. E., Porter, J. N., and Bates, D. E. "Single-Pulse Standoff Raman Detection of Chemicals from 120 m Distance during Daytime," Appl. Spectrosc. 2012. 66: 1279–1285.

Misra, A. K., Sharma, S. K., Chio, C. H., Lucey, P. G., and Lienert, B. "Pulsed remote Raman system for daytime measurements of mineral spectra," Spectrochim. Acta. Part A. 2005. 61: 2281-2287.

Misra, A. K., Sharma, S. K., Lucey, P. G. "Remote Raman Spectroscopic Detection of Minerals and Organics under Illuminated Conditions from a Distance of 10 m Using a Single 532 nm Laser Pulse." Appl. Spectrosc. 2006. 60(2): 223–228. doi:10.1366/000370206776023412.

Molaro, J. L., Choukroun, M., Phillips, C. B., Phelps, E. S., Hodyss, R., Mitchell, K. L., ... & Meirion-Griffith, G. (2019). The microstructural evolution of water ice in the solar system through sintering. Journal of Geophysical Research: Planets, 124(2), 243-277.

Moore, D. S. and Scharff, R. J. "Portable Raman Explosives Detection," Anal. Bioanal. Chem. 2009. 393; 1571–1578.

Moore, J., Black, G., Buratti, B., Phillips, C., Spencer, J., & Sullivan, R. "Surface properties, regolith, and landscape degradation." Europa. Tucson: University of Arizona Press, 2009. 329-349.

Murchie, S., Arvidson, R., Bedini, P., Beisser, K., Bibring, J. P., Bishop, J., . . . Wolff, M. (2007). Compact Reconnaissance Imaging Spectrometer for Mars (CRISM) on Mars Reconnaissance Orbiter (MRO). Journal of Geophysical Research, 112(E5). doi:10.1029/2006je002682

Mustard, J. F., Pieters, C. M., Isaacson, P. J., Head, J. W., Besse, S., Clark, R. N., . . . Tompkins, S. (2011). Compositional diversity and geologic insights of the Aristarchus crater from Moon Mineralogy Mapper data. Journal of Geophysical Research, 116. doi:10.1029/2010je003726

Myneni, S., Luo, Y., Näslund, L. Å, Cavalleri, M., Ojamäe, L., Ogasawara, H., Pelmenschikov, A., Wernet, P., Väterlein, P., Heske, C., Hussain, Z., Pettersson, L. G. M. and Nilsson, A. "Spectroscopic Probing of Local Hydrogen-Bonding Structures in Liquid Water." J. Phys.: Condensed Matter. 2002. 14(8): L213-L219doi:10.1088/0953-8984/14/8/106.

NASA ASTROBIOLOGY STRATEGY (2015) pp. 1-257. [accessed 2020 June 1]; https://nai.nasa.gov/media/medialibrary/2016/04/NASA_Astrobiology_Strategy_2015_FINAL_041216.pdf

Nelson, R. M., Shkuratov, Y., Boryta, M., Hapke, B. W., & Vandervoort, K. Understanding Europa's surface texture from remote sensing photopolarimetry. In 42nd COSPAR Scientific Assembly (Vol. 42). (2018).

Nordheim, T. A., Hand, K. P., Paranicas, C. Preservation of potential biosignatures in the shallow subsurface of Europa. Nature Astronomy 2, 673-679 (2018).

Oh, M.-K., Kang, H., Yu, N. E., Kim, B. H., Kim, J., Lee, J., and Hyung, G. W. "Ultimate Sensing Resolution of Water Temperature by Remote Raman Spectroscopy," Appl. Opt. 2015. 54: 2639–2646.

Paganini, L., Villanueva, G.L., Roth, L., A. M. Mandell, T. A. Hurford, K. D. Retherford and M. J. Mumma. A measurement of water vapour amid a largely quiescent environment on Europa. Nat Astron 4, 266–272 (2020). https://doi.org/10.1038/s41550-019-0933-6.

Pappalardo, R. T., Vance, S., Bagenal, F., Bills, B. G., Blaney, D. L., Blankenship, D. D., Brinckerhoff, W. B., Connerney, J. E., Hand, K. P., Hoehler, T. M., Leisner, J. S., Kurth, W. S., McGrath, M. A., Mellon, M. T., Moore, J. M., Patterson, G. W., Prockter, L. M.,

Senske, D. A., Schmidt, B. E., Shock, E. L., Smith, D. E., and Soderlund, K. M. Science potential from a Europa lander. Astrobiology 13, 740-773 (2013).

Parker, D. S. N., Zhang, F., Kim, Y. S., Kaiser, R. I., Landera, A., Kislov, V. V., Mebel, A. M., and Tielens, A. G. G. M. "Low Temperature Formation of Naphthalene and its Role in the Synthesis of PAHs (Polycyclic Aromatic Hydrocarbons) in the Interstellar Medium", Proc. Nat. Acad. Sci. 2012. 109: 53-58.

Petry, R., Schmitt, M., and Popp, J. "Raman spectroscopy—A Prospective Tool in the Life Sciences," Chem. Phys. Chem 4. 2003: 14–30.

Pierazzo, E., Chyba, C. F. Cometary Delivery of Biogenic Elements to Europa. Icarus 157, 120-127 (2002).

Pieters, C. M., Besse, S., Boardman, J., Buratti, B., Cheek, L., Clark, R. N., . . . Whitten, J. (2011). Mg-spinel lithology: A new rock type on the lunar farside. Journal of Geophysical Research, 116. doi:10.1029/2010je003727

Pieters, C. M., Canup, R., Kring, D., Head III, J. W., & Scott, D. R. (2018). Transformative Lunar Science. Solar System Exploration Research Vittual Institute (SSERVI).

Pieters, C. M., Goswami, J. N., Clark, R. N., Annadurai, M., Boardman, J., Buratti, B., et al. (2009). Character and Spatial Distribution of OH/H2O on the Surface of the Moon Seen by M3 on Chandrayaan-1. Science, 326(5952), 568.

Pieters, C. M., Goswami, J. N., Clark, R. N., Annadurai, M., Boardman, J., Buratti, B., . . . Varanasi, P. (2009). Character and Spatial Distribution of OH/H2O on the Surface of the Moon as Seen by M3 on Chandrayaan-1. Science, 326, 568-572.

Pieters, C., Boardman, J., Buratti, B., Clark, B., Green, R., Head III, J. W., . . . Tompkins, S. (2006). Characterizing the Mineralogy of Potential Lunar Landing Sites. International Lunar Conference.

Pieters, C.M. et al. (2009) Character and Spatial Distribution of OH/H2O on the Surface of the Moon Seen by M3 on Chandrayaan-1. Science, 326, 568-572.

Pieters, C.M. et al. (2014) Mg-Spinel on the Moon. American Mineralogist, Volume 99, pages 1893–1910, 2014.

Postberg, F., Clark, R.N., Hansen, C.J., Coates, A.J., Dalle Ore, C.M., Scipioni, F., Hedman, M. M. and Waite, J.H. (2018b) Plume and Surface Composition of Enceladus, in P. M. Schenk, R. N.Clark, A. Howett, A. J. Verbicer, J. H. Waite (eds) Enceladus and the Icy Moons of Saturn, 129-162. University of Arizona Press (2018 b).

Postberg, F., Kempf, S., Schmidt, J., Brilliantov, N., Beinsen, A., Abel, B., Buck, U. and Srama, R. Sodium salts in E-ring ice grains from an ocean below the surface of Enceladus. Nature 459, 1098-1101 (2009).

Quick, L. C., Barnouin, O. S., Prockter, L. M., Patterson, G. W. Constraints on the detection of cryovolcanic plumes on Europa, Planetary and Space Science, 86, 1-9 (2013), https://doi.org/10.1016/j.pss.2013.06.028.

Ralph D. Lorenz, Europa ocean sampling by plume flythrough: Astrobiological expectations, Icarus, Volume 267, 2016,Pages 217-219,https://doi.org/10.1016/j.icarus.2015.12.018.

Raman, C.V., "A Change of Wavelength in Light Scattering." Nature. 1928. 121: 619.

Reed, I.S.; Yu, X. Adaptive multiple-band CFAR detection of an optical pattern with unknown spectral distribution. IEEE Trans. Acoust. Speech Signal Process. 1990, 38, 1760–1770.

Roth, L., Saur, J., Retherford, K. D., Strobel, D. F., Feldman, P. D., McGrath, M. A., and Nimmo, F. "Transient Water Vapor at Europa's South Pole." Science 343, no. 6167. 171-74. (2014). https://dx.doi.org/10.1126/science.1247051.

Rull Pérez, F. and Martinez-Frias, J. "Raman Spectroscopy Goes to Mars," Spectrosc. Eur. 2006. 18(1): 18–21.

Rull Perez, F., Edwards, H., Rivas, A., and Drummond, L. "Fourier Transform Raman Spectroscopic Characterization of Pigments in the Mediaeval Rescoes at Convento de la Peregrina, Sahagun, Léon, Spain, part 1—Preliminary Study," J. Raman Spectrosc. 1999. 30: 301–305.

Rull, F., Maurice, S., Hutchinson, I., Moral, A., Perez, C., Diaz, C., Colombo, M., Belenguer, T., Lopez-Reyes, G., Sansano, A., Forni, O., Parot, Y., Striebig, N., Woodward, S., Howe, C., Tarcea, N., Rodriguez, P., Seoane, L., Santiago, A., Rodriguez-Prieto, J. A., Medina, J., Gallego, P., Canchal, R., Santamarıa, P., Ramos, G., and Vago, J. L.; on behalf of the RLS Team, "The Raman Laser Spectrometer for ExoMars Rover Mission to Mars". Astrobiology. 2017. 167(6-7): 627-654.

Rull, F., Vegas, A., Sansano, A., and Sobron, P. "Analysis of Arctic Ices by Remote Raman Spectroscopy," Spectrochim. Acta, Part A. 2011. 80(1): 148–155.

Schmidt, C. (2014). Raman spectroscopic determination of carbon speciation and quartz solubility in $H_2O + Na_2CO_3$ and $H_2O + NaHCO_3$ fluids to 600 °C and 1.53 GPa. Geochimica et Cosmochimica Acta, 145, 281-296. doi:10.1016/j.gca.2014.09.009

Sephton, M. A., Waite, J. H., Brockwell, T. G. How to Detect Life on Icy Moons. Astrobiology 18, 843-855 (2018).

Sharma, S. K., J. N. Porter, A.K. Misra, T. E. Acosta-Maeda, S. M. Angel, and C. P. McKay. Standoff Raman Spectroscopy for Future Europa Lander Missions. Journal of Raman Spectroscopy, (2019).

Sharma, S. K., Lucey, P. G., Ghosh, M., Hubble, H. W., and Horton, Keith A. "Stand-off Raman Spectroscopic Detection of Minerals on Planetary Surfaces." Spectrochim. Acta. Part A. 2003. 59(10): 2391-407.

Sharma, S. K., Misra, A. K., Acosta-Maeda, T. E., Lucey, P. G. "Time-Resolved Remote Raman and Fluorescence Spectrometers for Planetary Exploration." Laser Radar Technology and Applications XVII, Proc. SPIE, 2012. 8378:8378J/1-12. doi:10.1117/12.920955.

Sharma, S. K., Misra, A. K., Clegg, S. M., Barefield, J. E., Wiens, R. C., Acosta-Maedea, T. E., and Bates, D. E. "Remote-Raman Spectroscopic Study of Minerals under Supercritical CO_2 Relevant to Venus Exploration," Spectrochim. Acta. Part A. 2011. 80: 75–81.

Sharma, S. K., Misra, A. K., Lucey, P. G., and Lentz, R. C. F. "A Combined Remote Raman and LIBS instrument for Characterizing Minerals with 532 nm Laser Excitation," Spectrochim. Acta, Part A. 2009. 73; 468–476.

Sharma, S. K., Misra, A. K., Lucey, P. G., Angel, S. M., and Mckay, C. P. "Remote Pulsed Raman Spectroscopy of Inorganic and Organic Materials to a Radial Distance of 100 Meters." Appl. Spectrosc. 2006. 60(8); 871-876.

Sharma, S. K., Misra, A. K., Lucey, P. G., Angel, S. M., and McKay, C. P. "Remote Pulsed Raman Spectroscopy of Inorganic and Organic Materials to a Radial Distance of 100 Meters," Appl. Spectrosc. 2006. 60: 871–876.

Sharma, S., & Egan, M. (2019). Raman Spectroscopy: Theory and Laboratory Spectra of Geologic Materials. In J. Bishop, J. Bell III, & J. Moersch (Eds.), Remote Compositional Analysis: Techniques for Understanding Spectroscopy, Mineralogy, and Geochemistry of Planetary Surfaces (Cambridge Planetary Science, pp. 120-146). Cambridge: Cambridge University Press. doi:10.1017/9781316888872.008

Space Studies Board. "Vision and Voyages for Planetary Science in the Decade 2013-2022." The National Academies Press, Washington D.C., 2011. doi:10.17226/13117.

Stern, J. C., Sutter, B., Freissinet, C., Navarro-González, R., McKay, C. P., Archer Jr., P. D., Buch, A., Brunner, A. E., Coll, P., Eigenbrode, J. L., Fairen, A. G., Franza, B., Glavina, D. P., Kashyap, S., McAdam, A. C., Ming, D. W., Steele, A., Szopa, C., Wray, J. J., Martín-

Torres, F. J., Zorzano, M.-P., Conrad, P. G., Mahaffy, P. R., and the MSL Science Teams, "Evidence for Indigenous Nitrogen in Sedimentary and Aeolian Deposits from the Curiosity Rover Investigations at Gale Crater, Mars", Proc Nat. Acs Sci. USA. 2015. 112: 4245-4250.

Taylor, L. A., Pieters, C. M., Keller, L. P., Morris, R. V., & McKay, D. S. (2001). Lunar Mare Soils: Space weathering and the major effects of surface-correlated nanophase Fe. Journal of Geophysical Research: Planets, 106(E11), 27985-27999. doi:10.1029/2000je001402

Taylor, L. A., Pieters, C., Patchen, A., Taylor, D.-H., Morris, R. V., Keller, L. P., & McKay, D. S. (2003). Mineralogical Characterization of Lunar Highland Soils. Lunar and Planetary Science XXXIV.

Thompson, D. R., Leifer, I., Bovensmann, H., Eastwood, M., Fladeland, M., Frankenberg, C., Gerilowski, K., Green, R. O., Kratwurst, S., Krings, T., Luna, B., and Thorpe, A. K. (2015). Real-time remote detection and measurement for airborne imaging spectroscopy: a case study with methane, Atmos. Meas. Tech., 8, 4383-4397, https://doi.org/10.5194/amt-8-4383-2015.

Tomikawa, K., Kanno, H. Raman Study of Sulfuric Acid at Low Temperatures. Journal of Chemical Physics 102, 6082-6088 (1998).

Trumbo, S. K., Brown, M. E., & Hand, K. P. Sodium chloride on the surface of Europa. Science Advances, 5(6), eaaw7123. (2019). doi:10.1126/sciadv.aaw7123.

Truong, N., Monroe, A. A., Glein, C. R., Anbar, A. D., & Lunine, J. I. (2019). Decomposition of amino acids in water with application to in-situ measurements of Enceladus, Europa and other hydrothermally active icy ocean worlds. Icarus, 329, 140-147. doi:10.1016/j.icarus.2019.04.009

Van Gorp, B., Mouroulis, P., Blaney, D., Green, R. O., Ehlmann, B. L., & Rodriguez, J. I. (2014). Ultra-compact imaging spectrometer for remote,in situ, and microscopic planetary mineralogy. Journal of Applied Remote Sensing, 8(1). doi:10.1117/1.Jrs.8.084988

Vance, S. D., Hand, K. P., and Pappalardo, R. T. Geophysical controls of chemical disequilibria in Europa, Geophys. Res. Lett., 43, 4871–4879, (2016). doi:10.1002/2016GL068547.

Viviano-Beck, C. E., Seelos, F. P., Murchie, S. L., Kahn, E. G., Seelos, K. D., Taylor, H. W., . . . Morgan, M. F. (2014). Revised CRISM spectral parameters and summary products based on the currently detected mineral diversity on Mars. Journal of Geophysical Research: Planets, 119(6), 1403-1431. doi:10.1002/2014je004627

Vu, T. H., Hodyss, R., Choukroun, M., & Johnson, P. V. Chemistry of Frozen Sodium– Magnesium–Sulfate–Chloride Brines: Implications for Surface Expression of Europa's Ocean Composition. The Astrophysical Journal 816, (2016).

Wang, A., Freeman, J.J., Jolliff, B.L., and Chou, I.-M. "Sulfates on Mars: A Systematic Raman Spectroscopic Study of Hydration States of Magnesium Sulfates." Geochim. Cosmochim.Acta. 2006. 70(24): 6118–6135. doi:10.1016/j.gca.2006.05.022.

Wang, A., Jolliff, B. L., and Haskin, L. A. "Raman Spectroscopy as a Method for Mineral Identification on Lunar Robotic Exploration Missions," J. Geophys. Res. 1995. 100: 21189–21199.

Whalley, E. "A Detailed Assignment of the O–H Stretching Bands of Ice I." Canadian J. Chem.. 1977. 55(19): 3429–3441. doi:10.1139/v77-481.

Whitten, J., Head, J. W., Staid, M., Pieters, C. M., Mustard, J., Clark, R., . . . Taylor, L. Lunar mare deposits associated with the Orientale impact basin: New insights into mineralogy, history, mode of emplacement, and relation to Orientale Basin evolution from Moon Mineralogy Mapper (M3) data from Chandrayaan-1. Journal of Geophysical Research, 116. (2011). doi:10.1029/2010je003736

Wiens, R. C., Maurice, S., Barraclough, B., et al. "The ChemCam Instrument Suite on the Mars Science Laboratory (MSL) Rover: Body Unit and Combined System Tests." Space Sci Rev. 2012. 170: 167–227. doi:10.1007/s11214-012-9902-4

Wiens, R.C., Maurice, S., and Rull Perez, F. "The SuperCam Remote Sensing Instrument Suite for the Mars 2020 Rover: A Preview". Spectroscopy. 2017. 32(5): 50-55.

Zuber MT, Head JW, Smith DE, et al. Constraints on the volatile distribution within Shackleton crater at the lunar south pole. Nature. 486 (7403):378-381. 2012. doi:10.1038/nature11216.